Lu *et al*. *J Mater Inf* 2022;2:7
DOI: 10.20517/jmi.2022.07

Journal of Materials Informatics

Review

Open Access

Recent progress in the data-driven discovery of novel photovoltaic materials

Tian Lu[1], **Minjie Li**[2,3,*], **Wencong Lu**[1,2,3,*], **Tong-Yi Zhang**[1,*]

[1]Materials Genome Institute, Shanghai University, Shanghai 200444, China.
[2]Department of Chemistry, College of Sciences, Shanghai University, Shanghai 200444, China.
[3]Zhejiang Laboratory, Hangzhou 311100, Zhejiang, China.

***Correspondence to:** Minjie Li, Department of Chemistry, Shanghai University, No.99 Shangda Road, Shanghai 200444, China. E-mail: minjieli@shu.edu.cn; Wencong Lu, Materials Genome Institute, Shanghai University, No.99 Shangda Road, Shanghai 200444, China. E-mail: wclu@shu.edu.cn; Tong-Yi Zhang, Materials Genome Institute, Shanghai University, No.99 Shangda Road, Shanghai 200444, China. E-mail: zhangty@shu.edu.cn

How to cite this article: Lu T, Li M, Lu W, Zhang TY. Recent Progress in the Data-driven Discovery of Novel Photovoltaic Materials. *J Mater Inf* 2022;2:7. http://dx.doi.org/10.20517/jmi.2022.07

Received: 12 Apr 2022 **First Decision:** 6 May 2022 **Revised:** 20 May 2022 **Accepted:** 25 May 2022 **Published:** 22 Jun 2022

Academic Editor: Xingjun Liu **Copy Editor:** Tiantian Shi **Production Editor:** Tiantian Shi

Abstract

The discovery of new photovoltaic materials can facilitate technological progress in clean energy and hence benefit overall societal development. Machine learning (ML) and deep learning (DL) technologies integrated with domain knowledge are revolutionizing the traditional trial-and-error research paradigm that is associated with high costs, inefficiency, and significant human effort. This review provides an overview of the recent progress in the data-driven discovery of novel photovoltaic materials for perovskite, dye-sensitized and organic solar cells. The integral workflow of the ML/DL training progress is briefly introduced, covering data preparation, feature engineering, model building and their applications. The cutting-edge challenges and issues in the ML/DL workflow are summarized specifically for photovoltaic materials. Real examples are emphasized to illustrate how to utilize ML/DL techniques in the discovery of novel photovoltaic materials. The prospects and future directions of the data-driven discovery of novel photovoltaic materials are also provided.

Keywords: Machine learning, materials design, deep learning, photovoltaic materials, data-driven, perovskite solar cells, organic solar cells, dye-sensitized solar cells

INTRODUCTION

Due to their capability to convert clean and inexhaustible solar radiation to electricity directly, photovoltaic technologies, especially solar cells, have provided a new alternative to traditional fossil fuels, which suffer from issues of resource exhaustion and environmental pollution[1,2]. Though silicon (Si) solar cells have dominated the major commercial photovoltaic markets, as a result of their mature production process, superior stability, and outstanding power conversion efficiency (PCE), the development of Si solar cells has been critically hindered by the high expense of elevated purity Si resources and costly device fabrication[3,4]. This is evidenced by the continuous decline in their research publications, decreasing from 13% of all solar cell studies in 2013 to 6% in 2022 (until March), as shown in Figure 1A. New photovoltaic technologies are therefore urgently required to replace Si solar cells.

There are 3 extraordinary photovoltaic devices in the leading roles of third-generation solar cells, namely, perovskite solar cells (PSCs), dye-sensitized solar cells (DSSCs), and organic solar cells (OSCs), which exhibit their respective potential either in conversion efficiency, stability and/or low production costs, and thus their research contribution in terms of publications has grown from 18% in 2013 to 35% in 2022[5]. In particular, the development of PSCs, after the incubation period of 2009-2014, has been extremely rapid with a significant growth in device performance regarding PCE, from an initial 3.8%[6] to currently over 25.5%[7–10], which is competitive with that of Si-based devices. PSCs have therefore become the veritable superstar in the photovoltaic community and represented 19% in 2021 and even 21% in 2022 of all publications in this field. PSCs illustrate excellent optical and electronic properties, including tunable adjustable bandgaps, long carrier diffusion lengths, high light-absorption coefficients, low nonradiative loss, carrier mobility, and solution processability[11–13]. Despite their promising device performance, significant progress for PSCs is still required towards commercialization due to their low stability, reduced scalability, and potential environmental pollution caused by the use of lead in their chemical composition.

As the nominal parents of PSCs, DSSCs have drawn significant attention since their first report 30 years ago[14], with the merits of relatively low cost, eco-friendliness, structural flexibility, and good stability[15]. Compared to PSCs, DSSCs are much easier to scale up but have struggled with the persistent bottleneck of the relatively lower PCEs of ~14%[16]. This is why the research trend on DSSCs kept a high percent of ~12% of publications before 2014 but started to decrease with the discovery of PSCs in 2015. The early studies of OSCs can be traced from even five years earlier than DSSCs[17,18], with a much more continuous research trend of 7%-9% in the past decade. OSCs have their own various benefits of inexpensive production costs, solution possibility, low temperature possessing, structural flexibility, semi-transparency, suitability for large-scale roll-to-roll processing, and relatively high PCEs (> 18%)[19–22]. Ternary device structures of OSCs are usually employed in order to achieve sufficient photon harvesting and efficient cell performance, which, however, may cause difficulties regarding morphological control and lower open-circuit voltages[23].

In recent decades, tremendous experimental efforts have been dedicated to the fabrication and characterization of new photovoltaic materials for solar cells. Most approaches, however, are traditional trial-and-error methods based on expert experience and intuition, along with large costs in terms of time and human endeavor[24,25]. Computations, especially density functional theory (DFT)[26,27] -based calculations and molecular dynamics (MD)[28], have been exerted to accelerate experimental investigations and explore the relevant mechanisms behind experimentally observed behavior. Nonetheless, these quantum-based methods are largely restrained by contemporary computing powers that are not well qualified for large-scale simulations with satisfactory accuracy[29]. Like experiments and high-throughput experiments, computations and high-throughput computations also generate huge amounts of data. The data-driven machine learning (ML) and deep learning (DL) methods, as subfields of artificial intelligence (AI), are being quickly adopted by the materials community to fully utilize experimental and computational data to yield a new interdisciplinary field of materials informatics. Materials informatics has already achieved significant success in many branches of materials, such as electro-

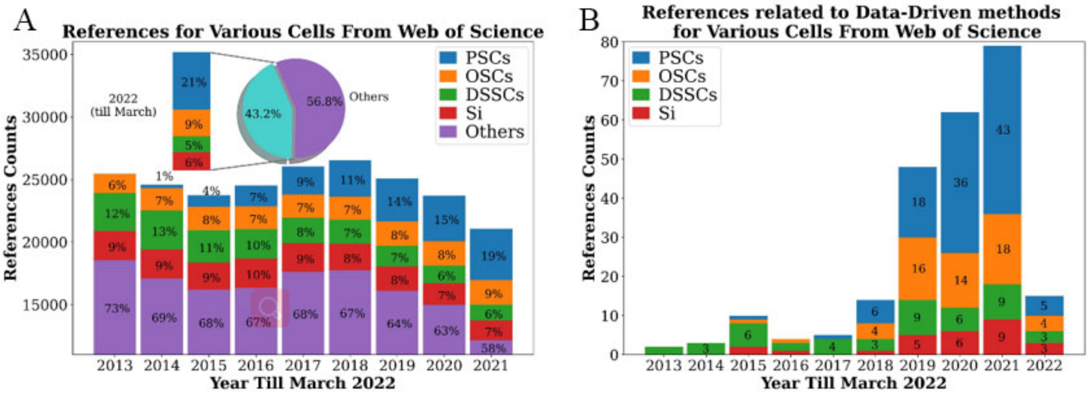

Figure 1. (A) Research trends for various types of solar cells from 2013 to 2022. The percentages in the histograms represent the percentages of each cell in the specific year. We used the search patterns "TS=('solar cell*') AND TS=('perovskite solar cell*')" for PSCs, and "TS=('solar cell*') AND TS=('organic solar cell*')" for OSCs, "TS=('solar cell*') AND TS=('dye-sensitized solar cell*')" for DSSCs and "TS=('solar cell*') AND TS=(Si)" for Si solar cells. (B) Research trends for ML and DL techniques for various solar cells from 2013 to 2022. The numbers in the histograms represent the numbers of references for each cell in the specific year. We added the term "TS=('machine learning' OR 'data mining' OR 'deep learning' OR 'QSPR' OR 'QSAR' OR 'quantitative structure-property relationship' OR 'quantitative structure-activity relationship')" to each search pattern in (A) for the respective solar cell.

catalysis, batteries, metal-organic frameworks, two-dimensional (2D) materials, polymers, metals, alloys, and so on[30–33]. Data-driven ML and DL technologies have advantages in catching up the relations between targeted properties and input variables[34]. Coherently integrating the data-driven approach with domain knowledge will make the black box more transparent, enhance ML and DL technologies more efficiently and boost the quantum jump from data to knowledge, thereby paving the way for novel materials discovery[35].

Materials informatics is developing extremely fast in various material fields, including photovoltaic materials. The total number of ML/DL-related studies of solar cells in 2021 was over 180, nearly nine times the number of 19 in 2015 and 50 times that of a decade ago, thereby evidencing the flourishing developing trend in this interdisciplinarity area. As shown in Figure 1B, the main contribution to this fast development is credited to the ML/DL research on PSCs, in which the number of publications increased from six in 2018 to 43 in 2021. The same trend can be observed in OSCs, whose explosive growth was centered in 2019-2021. The related studies on DSSCs show a relatively steady development, with an annual publication number of three to seven. Considering the momentary development of materials informatics in photovoltaic materials and the hundreds of pioneering achievements to accelerate the discovery of photovoltaic materials, it is necessary and timely to review the progress of materials informatics in photovoltaic materials.

In this review, we focus on the recent applications of data-driven methods in the photovoltaic materials of PSCs, DSSCs, and OSCs. We first portray the integral workflow of ML and DL in section "MACHINE LEARNING AND DEEP LEARNING WORKFLOW" (section 2), emphasizing their essential operations in different stages from the preparation of data towards the evaluation of ML/DL models. Real cases are then illustrated in section "RECENT PROGRESS OF DATA-DRIVEN METHODS" (section 3) as examples to show how ML/DL technologies can be used to discover novel photovoltaic materials. The final section addresses the prospects and future directions of material informatics in photovoltaic materials.

MACHINE LEARNING AND DEEP LEARNING WORKFLOW

Figure 2 shows the adaptive design workflow of ML/DL, where domain knowledge, i.e., expert professional knowledge, is the hub. ML/DL work on data, and thus data preparation is the essential and fundamental step. Data are composited by input variables, known as features in ML/DL, and output variables, which are

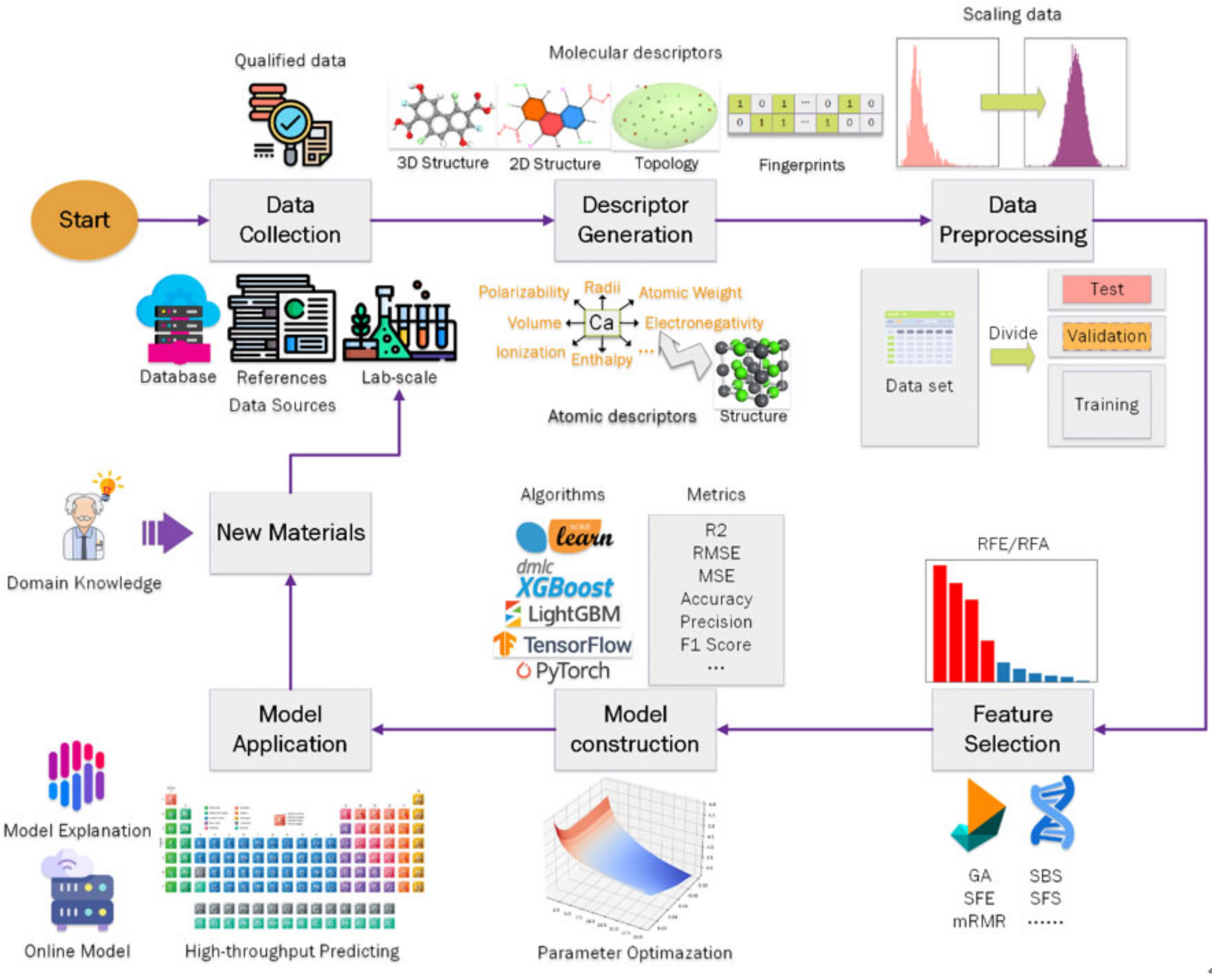

Figure 2. Diagram of ML/DL workflow. RFE/RFA: Recursive feature elimination/addition; GA: generic algorithm; SFE: sequential feature elimination; mRMR: maximum relevance minimum redundancy; SBS: sequential backward selection; SFS: sequential forward selection; R^2: determination coefficient; RMSE: root mean squared error; MSE: mean squared error.

materials properties or other materials characteristics of interest. Features and feature space are two crucial issues in ML/DL, and thus feature engineering must be conducted, which involves the preprocessing, filtering, and generating of features. After that, ML/DL models are developed with ML/DL algorithms. Based on the ML/DL models, recommendations are given to guide the next experiments and/or calculations. The results of the experiments and/or calculations are then put into a database, which iteratively grows until reaching the design goal.

Data collection

The goal of the data-driven procedure is to find the underlying correlations between the target properties and input features via ML/DL algorithms. To avoid "garbage in garbage out" in ML/DL practitioners, a reasonable dataset matters more than the data-driven algorithms, suggesting that more efforts are demanded to cleanse and filter the original dataset[36–38].

Qualified datasets

A reasonable dataset is determined by its data quality, namely, the veracity of each sample, which correlates the portions of inconsistent, incorrect, and missing data. Inconsistent data refer to samples with the same chemical composition, structures, and the same processing conditions but that exhibit diverse values of their target, in

Table 1. Popular online databases

Database	Link
Materials project [52]	https://materialsproject.org/
Inorganic crystal structure database (ICSD) [53]	https://www.psds.ac.uk/icsd
Open quantum materials database (OQMD) [54,55]	https://oqmd.org/
Materials platform for data science (MPDS) [56]	https://mpds.io/
Materials data specification (MDS) [58]	https://github.com/conchsk/Materials-Data-Specification
Automatic-flow for materials discovery (AFLOWLIB)	http://aflowlib.org
American mineralogist crystal structure database	http://rruff.geo.arizona.edu/AMS/amcsd.php
Cambridge crystallographic data center (CCDC) [61]	www.ccdc.cam.ac.uk/pages/Home.aspx
Chemspider	www.chemspider.com
Computational materials repository (CMR)	http://cmr.fysik.dtu.dk/
Crystallography open database (COD) [62]	www.crystallography.net
Database of materials properties (MatDat)	www.matdat.com
NIMS materials database (MatNavi)	https://mits.nims.go.jp/
NanoHUB	https://nanohub.org/
Total materia	www.totalmateria.com
Pauling file	http://paulingfile.com
PubChem	https://pubchem.ncbi.nlm.nih.gov/
Materials genome engineering databases (MGED) [57]	https://www.mgedata.cn/

which their mean value can be filled if the difference of the diverse values is acceptable [39]. In the converse case, part of the inconsistent data can be presumed based on domain knowledge and/or statistical analysis as the incorrect data, i.e., the outliers. Besides the simple principle "obey the majority", statistical criteria/methods, like the standard deviation, Student's t test [40,41], $F-$test [42] and ML-based methods, including the local outliers factor (LOF) [43], isolation forest (iForest) [44], minimum covariance determinant (MCD) method [45,46] and angle-based outlier detection (ABOD), can be used to detect the incorrect data [45,47–49].

In the LOF method, the density of neighboring samples for every one of the data is calculated, and the outliers are defined by the ones with their neighbor density lower than a preset threshold. The iForest method builds up a set of decision trees and evaluates the average depth of each sample. Due to the diverse feature values from the normal ones, the outliers are probably isolated at the terminal nodes close to the root of a tree and hence can be defined by the leaf depth smaller than a pre-defined threshold. The MCD method utilizes the Mahalanobis distance based on the covariance matrix of the dataset to evaluate each sample and defines the outliers by the Mahalanobis distance larger than a designated value. In the ABOD method, each sample corresponding to one point in feature space is evaluated by the variance of the angles between vectors from it to every one of the other points. The angles of a normal point in a cluster tend to differ widely and exhibit a relatively larger variance, while an outlier owns the integrally small angle and can be defined by the variance lower than a prefixed cutoff value. The details of these four algorithms are are given in Section S1, Tables S2 and S3, and Figures S1 and S2 of the supporting information, along with the code application on how to perform a fast search for outliers. Regarding the missing values of some descriptors, we might drop the sample or descriptor that contains one or more missing values, or fill in the average values, while some cutting-edge ML algorithms, for example, extreme gradient boosting (XGBoost) [50] and categorical boosting (CatBoost) [51], can handle the missing values internally.

Data sources

Databases

Generally, a dataset can be collected from three sources: currently available databases, publications, and lab-scale data. There are several publicly available experimental and computational databases, covering numeric (properties and processing conditions) and image [X-ray diffraction (XRD) and X-ray photoelectron spectroscopy (XPS)] data, such as those listed in Table 1, including the Materials Project [52], Inorganic Crystal Structure Database (ICSD) [53], Open Quantum Materials Database (OQMD) [54,55], Materials Platform for Data Science (MPDS) [56], Materials Genome Engineering Databases (MGED) [57], Materials Data Specification (MDS) [58] and others [58–62].

Significant time can be saved by building ML models using databases instead of collecting samples from publications. As a result, researchers can instead dedicate their efforts to selecting, comparing and cascading the ML algorithms. For instance, Rafael *et al.*[63] proposed an automatic chemical design approach by combining the variational autoencoder (VAE) framework and the open-source cheminformatics suite RDKit[64]. Two autoencoder systems were carefully designed and fitted based on one dataset with 108,000 molecules from QM9[65] and another dataset with 250,000 drug-like commercially available molecules extracted at random from ZINC[66]. The most publicly available databases usually contain general information without specific properties and processing conditions. For example, it is difficult to obtain PCE data from the OQMD database. In this context, databases for specific types of materials might be more important for their particular fields[31]. The Harvard Clean Energy Project (CEP) is a distributed computing effort for screening organic photovoltaic candidates carried out by volunteers connected to the IBM World Community Grid[67], which has provided 1.3 million donor materials for non-fullerene materials[68]. The NIMS Materials Database (MatNavi) aims to contribute to the development of new materials and the selection of materials, and covers polymers, inorganics, metallics and their computational properties. The Harvard Organic Photovoltaic Dataset (HOPV15) is formed on the CEP and has assembled experimental photovoltaic structures from the literature along with their quantum-chemical calculations performed over a range of conformers[69]. Venkatraman *et al.* constructed the DSSCDB (DSSC database) to provide over 4000 synthesized sensitizer dyes with the reported device details, such as performance and experimental processing conditions[70].

Publication data

Collecting data from publications is the second choice, especially when there is a lack of accomplished, authoritative, and professional databases in the concerned fields. Odabası *et al.* presented an overview and analysis of the 1921 organo-lead-halide PSC device performances that were accumulated from 800 publications between 2013 and 2018[71]. By extending the dimensions of the dataset, more assessments on the reproducibility, hysteresis, and stability of the extended dataset using association rule mining methods were further carried out in 2020[72,73] and 2021[74]. Compared to the direct usage of databases, it is noteworthy that significantly more endeavors are urgently required to check the consistency and integrity of the collected data before ML/DL model building.

Lab-scale data

Lab-scale experiments and computations in individual research labs are the most fundamental and widely distributed data sources and generate original and valuable data. Coinciding with the developments in high-throughput experiments and computations, the scale of data is growing fast, especially the size of calculated data, which are scaled up quickly through high-throughput platforms and various quantum-based software like Materials Studio (MS)[75], the Vienna Ab initio Simulation Package (VASP)[76–79] and the Gaussian suite[80]. In the work of Hartono *et al.*, 21 organic salts were deposited as capping-layer materials on the top of a thick film of methylammonium lead iodide ($MAPbI_3$) to investigate the influence of capping layers on the $MAPbI_3$ stability[81]. The SHapley Additive exPlanations (SHAP) tool[82] was used to determine two important factors, namely, the polar surface area and the number of H-bond donors. Furthermore, Saidi *et al.* systematically produced a dataset composed of 862 halide perovskite materials with their optimized structures and bandgaps via DFT to develop ML models[83]. With developments in robotics, experiments can be processed automatically, and hence robot-based experimental lab-scale data are also expected to be scaled up exponentially. For instance, Zhao *et al.* utilized a high-throughput robot (HTRobot) system coupled with ML and robot learning to synthesize, characterize and analyze over 1000 materials of interest[84]. Further ML analysis of the generated data yielded a correlation between temperature and stability.

Descriptor generation

Descriptors, also known as features, and search space are the two crucial issues in ML. The descriptor types of material structures depend on whether the structures are aperiodic or periodic. Aperiodic structures can be stored in the file types of the simplified molecular-input line-entry system (SMILES) or molecular file (MOL), while periodic ones can be dumped into crystallographic information files (CIFs). Aperiodic system structures, including the pure organic structures of photovoltaic absorbers in OSCs, DSSCs, and metal-organic frameworks (MOF), can be depicted using molecular descriptors, while atomic and crystal structural descriptors are generally used for periodic systems, e.g., the crystal perovskite structures in PSCs.

Molecular descriptors

Thousands of molecular descriptors in dozens of types have been proposed and generated with assorted tools[85]. Taking one of these tools, Dragon software[86,87], as an example, we can generate 5270 descriptors in 30 types [Table S1], from the simplest 0-dimensional (0D) constitutional indices to the most abstract and complicated 3-dimensional (3D) spatial representations. The optimized structures via DFT calculations are needed for the generation of 3D descriptors, while the other descriptors can be based on only 2D structures, such as in the SMILE format and its enhanced versions, such as Selfies[88].

The development of an interpretable ML model requires simple and understandable descriptors, e.g., the descriptors marked as "Easy" in Table S1. Kar and co-workers[89] generated, using Dragon 6 software, 248 simple descriptors covering constitutional indices, ring descriptors, topological indices, connectivity indices, functional group counts, atom-type E-state indices, and 3D-atom pairs from the optimized structures for 273 collected arylamine organic dyes that were divided into 11 groups. Eleven linear regression models with interpretative features were then developed to predict PCE values with robust performances, and 29 new materials were accordingly designed with higher predicted PCE values. In 2020, Krishna *et al.*[90] collected over 1200 dyes from seven classes and generated only 2D descriptors from Dragon 7[86] and PaDEL-descriptor 2.21 software[91]. Eight linear models targeting the PCEs for each structure type were built along with their detailed feature interpretations, while ten new materials were designed with better predicted target values. Our group also has conducted relevant studies, especially on the interpretation of more abstract descriptors[92,93]. In our work[92,93], 3 hardly interpretable descriptors were successfully unveiled in the relations between the structures of sensitizers and their PCE values, as illustrated in Section S2, where Mor14p and Mor24m could be explained in favor of $C_{sp3}-S$, $C_{sp} \equiv C_{sp}$, $C_{sp2} = C_{sp2}$ and C-O bonds rather than the $C_{sp3} - C_{sp3}$ bond. R2s depicts that the sensitizer structures should have a lower density of geometrically marginal atoms, owing to the stronger electronegativity or higher bond order of the R=O, R−F, and R≡N bonds.

Fingerprints (FPs), as defined by Shemetulskis *et al.*, are the fixed size Boolean vectors that encode molecules by exploding their structures in all the possible substructure patterns under a given set of rules[94]. The most widely-used types are the path-based FPs that represent the substructures as linear chains of connected atoms and the extended connectivity fingerprints (ECFP) that use a variant of Morgan's extended connectivity algorithm[94–97].

FPs were originally introduced for fast database searching by evaluating the similarity/diversity between compounds. In recent years, FPs have been integrated into tools like Dragon software[86] and RDKit[64] and also applied in ML models for various organic systems, such as sensitizers in OSCs and DSSCs. Sun *et al.* used FPs, images, SMILE strings, and structural descriptors to depict the structures of 1719 organic photovoltaic donor materials collected from publications[98]. The random forest (RF) model with FPs achieved the highest accuracy of 86.67% in the classification task to identify the binary categories with a 10% PCE as the boundary. Kranthiraja *et al.* generated ECFPs for a collection of 556 samples of organic photovoltaic materials[99]. A RF model targeting PCEs was trained to yield a correlation coefficient (ρ) of 0.86 in leave-one-out cross-validation (LOOCV).

Table 2. Bond parameters arranged by Nianyi Chen

Bond parameter	Description
Ionic radius [Table S4]	Ionic radii for elements sand some chemical fragments
Covalent radius [Table S5]	Covalent radii for elements
Ionization energy [Table S6]	Ionization energies for elements along with different degrees from I to VIII
Metal radius [Table S7]	Metal radii of the metal atoms in their elemental metal
Valence electron to covalent radius ratio [Table S8]	The ratio of covalent radius [Table S5] divided by valence electron number
Electronegativity [Table S9]	Electronegativity for elements
Equivalent conductance [Table S10]	Equivalent conductance for molten chloride when the materials are at their melting point

Atomic descriptors

Compared to organic materials, periodic systems are dependent on their atomic and crystal structural descriptors. Atomic descriptors are publicly accessible in the Mendeleev package[100], Villars database[56], and RDKit[64], while structural descriptors are extracted from quantum-optimized crystal structures. Li *et al.*[101] employed the Python Materials Genomics (pymatgen) package[102] to obtain the atomic information and crystal structural parameters for 1593 ABO_3 perovskites sourced from the Materials Project[52]. The atomic descriptors included the atom number, atom mass, Pauling electronegativity, melting point, and electron numbers in valence orbitals, while the structural features included the octahedral distortion and bond lengths and angles. Several robust models were established to predict bandgaps, and one champion gradient boosting machine (GBM) model was obtained with a determination coefficient (R^2) of 0.855. Pilania *et al.* used the Shannon ionic radii, tolerance factor, octahedral factor, bond valence, electronegativity, and orbital radii of the atoms in ABX_3 perovskite materials to describe their structures[103]. They fitted a support vector machine (SVM) model with an accuracy score for a test set of 89.60% to determine the formability of the ABX_3 materials.

In addition to the public resources mentioned above, one very early work accomplished by Chen[104] also investigated the atomic descriptors (also described as the atomic parameters or parametric functions of chemical bonds) covering ionic radius, covalent radius, ionization energy, metal radius, ratio of valence electron to covalent radius, electronegativity, and equivalent conductance, as shown in Table 2. Chen not only assembled the bond parameters from the works of Slater[105], Belov[106], Pauling[107], Quill[108], Zachariasen[109], Sanderson[110], and Goldschmidt[111], but also reproduced and complemented the results with quantum calculations. The details of the atomic parameters have been extracted from Chen's work and provided in Section S3, which have been utilized in ML[112].

Such atomic descriptors might not be compatible with hybrid organic-inorganic perovskite (HOIP) structures due to the lack of relevant organic molecule properties for the A site (considering the HOIP chemical formula of ABX_3). Saidi *et al.*[83] supplemented the basic properties of 18 organic A-site ions for their 862 generated lab-scale data samples, including the first and second ionization energies, electron affinities, electric dipole, and molecular sizes, but still lacked most properties, such as the chemical potential, boiling temperature, enthalpy vaporization, ionic radii, volume, density and evaporation heat, which can be estimated based on theoretical methods[113–115]. In our developing Python package, these missing properties were supplemented for 80 organic ions and are also publicly accessible[116].

Other forms of representation

In addition to the descriptors discussed above, images are also one of the promising media to represent structures. Sun *et al.* fed a deep neural network with the images of chemical structures to classify the performances of organic solar cells with an accuracy of 91.02%[117]. Other image data from, for example, XRD and XPS, may also have the potential to represent structures, but few publications have been reported so far.

3D atomic coordinates can also be utilized as input values directly. The graph convolutional neural network (GCNN) is a new framework in deep learning for representing periodic crystal systems that are usually based on the coordinates in quantum-based optimized structures[118,119]. The GCNN treats the input crystal structures as a relational graph in which each atom is viewed as a node, and the connection relation between atoms is regarded as an edge. The model learns and updates the node and edge information in the crystal graph and finally deduces the relations between the coordinates and the output. Xie *et al.*[120] trained a GCNN model to predict various quantum-based properties of crystal structures extracted from the Materials Project[52], achieving mean absolute errors of 0.004-0.018 log(GPa) for the bulk/shear moduli and 0.097-0.212 eV for the formation energy and bandgap.

Another method to improve the information quality of features is to utilize symbolic methods that can generate a massive set of descriptors using combinations of the algebraic functions applied to existing features by relevant tools such as gplearn[121], DEAP[122] and the sure independence screening and sparsifying operator (SISSO)[123]. For instance, Bartel *et al.* successfully discovered an improved tolerance factor for the formability prediction of perovskites using the SISSO[124].

Data preprocessing

The collected data must be preprocessed to check their consistency and noise, especially for the same experimental data with the same testing conditions reported by different researchers. In addition, string variables that contain not just numbers but also other alphabetic characters (typically represented as categorical variables, e.g., lattice structures of hexagonal, tetragonal and cubic) are usually coded into integers by applying coding algorithms such as the one-hot encoder. If 2 variables are highly correlated, one of them should be removed to reduce the redundancy.

Scaling data is one of the prerequisite steps in data preprocessing to transform the input values into the same range, e.g., 0 to 1, which is optional for the tree-based algorithms that are insensitive to variable ranges. Several common scaling methods are accessible in the Python package scikit-learn (sklearn)[125]. For example, the standardization method is the most widely used and transforms data to the center with a zero mean and unit variance. Min-max scaling transforms the variables to lie between a given minimum and maximum value, often between 0 and 1.

The third important preprocessing step is to randomly divide a whole dataset into three subsets, usually by arranging a training set for building models, a validating set for evaluation while tuning model hyperparameters, and a test set for final evaluation of the model predicting performance. If the whole dataset is sufficiently large, the three subsets should possess the same distributions as the whole dataset[126,127]. However, the random splitting method does not operate well in relatively smaller and/or sparsely populated data, and hence the trained model tends to misjudge the test samples. Thus, when encountering a small dataset, the K-fold cross validation (K-CV) can be used to replace the validation set. In the K-CV method, the sample sets are randomly divided into K folds, with one of the folds used as the validating set and the rest of the folds acting as the training set. The divided training and validating sets are conducted K-times such that each of the K-fold data is used as a validating set once, and the average performances of the K models are taken as the trained ML model. If the fold number K is equivalent to the number of samples, then each fold contains only one of the samples and the method is deemed LOOCV.

Feature selection

The next crucial step is the feature selection to determine the critical features highly related to the target values and eliminate the redundant variables. Generally, feature selection methods can be classified into three types, namely, filter, wrapper, and embedded methods[128].

Filter-type methods evaluate variables that only rely on the general characteristics of the dataset and do not involve any ML algorithm, which is advantageous for low computing costs[38,129]. For instance, the minimum redundancy maximum relevance method (mRMR)[130–132] selects the optimal features by inspecting the relevance between the features and the target, and the redundancy among features. The maximum relevance is revealed by searching for the features that have the largest mutual information to the target $\boldsymbol{y}$, which satisfies the following equation:

$$\max D\left(\boldsymbol{S}_m, \boldsymbol{y}\right); D = \frac{1}{m} \sum_{\boldsymbol{x}_i \in \boldsymbol{S}_m} I\left(\boldsymbol{x}_i, \boldsymbol{y}\right) \tag{1}$$

where $\boldsymbol{S}_m$ represents the selected set comprising m features $\{\boldsymbol{x}_i, i = 1, \ldots, m\}$ and $I(\boldsymbol{x}_i, \boldsymbol{y})$ evaluates the mutual information between $\boldsymbol{x}_i$ and $\boldsymbol{y}$ as follows:

$$I\left(\boldsymbol{x}_i, \boldsymbol{y}\right) = \iint p\left(\boldsymbol{x}_i, \boldsymbol{y}\right) \log \frac{p\left(\boldsymbol{x}_i, \boldsymbol{y}\right)}{p\left(\boldsymbol{x}_i\right) p(\boldsymbol{y})} d\boldsymbol{x}_i d\boldsymbol{y} \tag{2}$$

The redundant information among the features in $\boldsymbol{S}_m$ is restrained by minimizing their mutual information as follows:

$$\min R\left(\boldsymbol{S}_m\right); R = \frac{1}{\left|\boldsymbol{S}_m\right|^2} \sum_{\boldsymbol{x}_i, \boldsymbol{x}_j \in \boldsymbol{S}_m} I\left(\boldsymbol{x}_i, \boldsymbol{x}_j\right) \tag{3}$$

where $I(\boldsymbol{x}_i, \boldsymbol{x}_j)$ evaluates the mutual information between $\boldsymbol{x}_i$ and $\boldsymbol{x}_j$:

$$I\left(\boldsymbol{x}_i, \boldsymbol{x}_j\right) = \iint p\left(\boldsymbol{x}_i, \boldsymbol{y}\right) \log \frac{p\left(\boldsymbol{x}_i, \boldsymbol{x}_j\right)}{p\left(\boldsymbol{x}_i\right) p\left(\boldsymbol{x}_j\right)} d\boldsymbol{x}_i d\boldsymbol{x}_j \tag{4}$$

Therefore, we can combine Equations (1) and (3) and consider the following simplest form to optimize them simultaneously:

$$\max(D - R) \tag{5}$$

Using Equation (5), Gallego *et al.*[132] gave one of the simplest algorithms as follows:

(1) Select one feature.
(2) Calculate its mutual information with the target as the relevance.
(3) Calculate its mean mutual information with other features as the redundance.
(4) Determine the difference between the relevance and redundancy as the mRMR score.
(5) Rank the features based on score.

After ranking the features by mRMR scores, one might propose a threshold and select features where the mRMR scores are higher than the threshold. Furthermore, mRMR scores can be combined with an ML model to select features. For example, based on the features ranked by the mRMR score, the recursive feature addition (RFA)[133] procedure can be used to determine the best feature subset by adding or removing one or more features, as follows:

(1) Select the top feature in the ranked features.
(2) Train and evaluate an ML model.
(3) Select the top two features in the ranked features to evaluate the new model.
(4) Subsequently, select the top three, four, five, and so on features in the ranked features and evaluate the new model, which results in the optimal feature subset with the best model performance.

The opposite recursive feature elimination (RFE) performs the same procedure but starts from the full feature set and eliminates features from the inverse order. By combining the mRMR filter method and the RFA/RFE procedure, an optimal feature subset for the model construction can be obtained, while the mRMR can be alternated by other filter methods, such as the variance threshold, mutual information, and chi-squared test methods[128].

Differentiating from filter types, wrapper methods select features depending on the model performance of an ML algorithm and typically iteratively repeat two steps: (1) searching for a feature subset; (2) evaluating the model performance with the feature subset, with the best performance corresponding to an optimal feature subset. In the typical representative genetic algorithm (GA)[122,134–137] method, each feature subset is regarded as a chromosome and has its own fitness that refers to the model performance of a specified algorithm. The superior/inferior chromosomes are retained/discarded, while new chromosomes are regenerated in each iterative step (known as generation) by mutating and crossing over. The detailed procedure of a GA is as follows:

(1) Generate a population composed of chromosomes. Each chromosome represents a feature subset.
(2) Evaluate chromosomes in this population by an ML model with a loss function. The model performance is set as the score for each chromosome.
(3) Deprecate the chromosomes with low scores.
(4) Crossover a randomly selected pair of chromosomes by exchanging their subparts to generate two new chromosomes and supplement the population.
(5) Mutate a randomly selected chromosome (usually $< 1\%$) by slightly altering part of its features to generate one new chromosome and supplement the population.
(6) Repeat steps (2)-(5) until the maximum step is reached.

Another widely used wrapper type is sequential forward selection (SFS) and its backward counterpart (SBS)[138]. SFS starts with one feature and finds the best feature that can maximize the performance of a model trained by one feature only, where, in contrast to RFA, every one feature is chosen randomly or iteratively. The second feature (every feature is chosen randomly in the rest features) is then added, the model is trained by two features, and the best second feature is selected. The procedure continues until the best performance is found by testing, which finally selects the desired features. SBS follows the same concept but from the full feature set and removes one feature that can maximize the model performance.

Embedded methods perform the feature selection in the process of training ML models and are specific to some ML algorithms that can export feature scores internally, e.g., tree-based algorithms (decision trees, RFs, and so on)[129,139]. When constructing a decision tree structure, the change in the Gini index caused by each feature is calculated and the features with high influence on the Gini index can be chosen for the selected set to train the decision tree model[140]. In addition, in the RF algorithm, multiple decision tree models are combined together, and the important features are determined by the average entropies from the sub-trees. In this regard, the features are sorted by Gini entropies in tree models and the feature subset is then selected via the RFA or RFE procedure. For example, Wen *et al.* employed embedded methods by combining RFE and tree-based models to select the features, which led to up to nine features remaining[141]. Li *et al.* adopted the same method to filter the optimal instrumental features for the bandgap of ABO_3 perovskites, in which the model could reach a stable R^2 value of 0.94 in cross validation with the selected 24 features[101].

The contributions of features to model predictions can be evaluated by SHAP values[82,142] Given a full feature set T_n composed of n features and a trained ML model (or a fitness function) f that takes a feature set S comprising $m(m \leq n)$ features as inputs and exports a prediction $f(S)$, the Shapley value ψ_i of a feature $\boldsymbol{x}_i$ is hence defined as follows:

$$\psi_i = \sum_{S \in \{T_n | \boldsymbol{x}_i\}} \frac{m!(n-m-1)!}{n!} \left[f\left(S \cup \{\boldsymbol{x}_i\}\right) - f(S) \right] \tag{6}$$

where $S \in \{N|\boldsymbol{x}_i\}$ indicates that S will traverse all the feature subset from the total set T_n but exclude the feature $\boldsymbol{x}_i$. The sum of the absolute SHAP values over the entire dataset of a feature represents the feature contribution and hence is used to rank the features. In one of our recent works[143], the SHAP method was used to determine six and four optimal features for the XGBoost and GBM classification models, respectively, rendering an over 85% test accuracy.

ML model construction

We now consider the core stage to select a suitable data-driven model for describing the relationship between the features and properties comprehensively, which also can be regarded as establishing a mapping function with multiple inputs and one or multiple outputs using ML/DL techniques. Benefitting from the decades of efforts taken by scientists in the fields of computer science, mathematics, and other related fields, abundant choices of user-friendly ML/DL algorithms [Table 3] with powerful predictivity have been publicly distributed and widely used, involving the typical tools, such as sklearn[125], XGBoost[50], LightGBM[144], PyTorch[145], and TensorFlow[146], which help materials scientists focus on exploiting feature spaces.

ML algorithms

Linear model

Linear regression. One traditional but still widely used algorithm is linear regression (LR), which expects the target value to be a linear combination of the features. A linear model is usually fitted by reducing the residual sum of squares between the observed and approximate target values via the ordinary least square method. In spite of its simplicity, there are still a large number of applications in photovoltaic fields[89,90,92,147–149]. For example, in the works of Kar[89,90,150–153], the LR algorithm was largely employed to fit multiple robust linear models for DSSCs.

Logistic regression classification. Logistic regression classification (LRC) is proposed to complement the classification form of LR by introducing a logistic function to predict the probability of a certain label[154–156]. Yu *et al*. built up an LRC model to determine whether a perovskite film exists after post-treatment, which led to a competitive test accuracy of 84% to 86% of the SVM[157].

Lasso and ridge regression. To reduce the overfitting problem of LR, the L1 regularization penalty is imposed into the calculation for the residual sum to form the lasso regression[158,159], while the L2 regularization penalty is expected to obtain the ridge regression (RR)[160]. In the work of Li *et al*., the lasso model, which was fitted to predict the formation energy of hypothetical perovskite materials based on only composition and stoichiometry information, exhibited a 10-fold cross-validation R^2 of 0.75, which was close to the value for RF of 0.80[161]. Stoddard *et al*. trained LR, RR, and lasso models to predict the time when the carrier diffusion length of $\mathrm{MAPbI_3}$ dropped to 85% of its initial value with a mean test error of 12.8%[162]. After applying a kernel trick into the RR algorithm, the kernel ridge regression (KRR) can be formed. Padula *et al*. employed KRR to perform multiple models based on electronic properties and FPs to predict the device performances, in which the model targeting PCE values had the largest ρ value of 0.68[163].

Decision trees

The so-called classification and regression tree (CART) algorithms, also known as decision trees, construct a tree-like structure by a binary recursive partitioning procedure capable of processing continuous and categorical features. The data samples are partitioned recursively into the binary nodes in each step (known as depth) by making a decision based on feature attributes until the number reduces to zero or the depth reaches a specified maximum[164]. Given the naive operating rule, it is simple to understand and interpret CART models by visualizing their tree structures. For example, Paul *et al*. trained a decision tree model for inorganic-organic hybrid materials to gain more deep insights into the influence of experimental conditions and perovskite properties on the reaction outcomes[165].

Table 3. Popular ML/DL algorithms for materials design

Algorithm Category	Derived Algorithm	ML Task Type	Comment/Trait
Linear model	Linear regression (LR)	Regression	Traditional but still widely used
	Logistic regression classification (LRC)[154–156]	Classification	Introduce logistic function into LR
	Lasso regression[158,159]	Regression	Introduce L1 regularization penalty into LR
	Ridge regression (RR)[160]	Regression	Introduce L2 regularization penalty into LR
Decision tree	Iterative Dichotomiser 3 (ID3)[222]	Classification	Use entropy to build decision tree
	C4.5[223]	Classification	Use entropy gain ratio to build decision tree
	Classification and Regression Tree (CART)[164]	Regression and classification	Use Gini entropy to build decision tree. Usually, the term of decision tree refers to CART algorithm
Ensemble trees (Averaging approach)	Pasting[167]	Regression and classification	Multiple trees are parallelly trained on randomized sample subsets without replacement
	Bagging[168]	Regression and classification	Multiple trees are parallelly trained on randomized sample subsets with replacement
	Random subspaces[169]	Regression and classification	Multiple trees are parallelly trained on randomized feature subsets with replacement
	Random forest (RF)[170]	Regression and classification	Multiple trees are parallelly trained on randomized samples and feature subsets with replacement
Ensemble trees (Boosting approach)	Adaboost[172]	Regression and classification	Multiple trees are sequentially trained to optimize sample weights
	Gradient boosting machine (GBM)[173]	Regression and classification	Multiple trees are sequentially trained to eliminate the bias of previous trees
	XGBoost[50]	Regression and classification	Introduce second-order Taylor approximation and L2 regularization into GBM
	Light gradient boosting machine (LightGBM)[174]	Regression and classification	Introduce gradient-based one-side sampling and exclusive feature bundling to GBM
	CatBoost[51,175]	Regression and classification	Adopt ordering principle into GBM
Support vector machine (SVM)[48,177,178]	Support vector regression (SVR)	Regression	A "must-try" and widely used algorithm. SVM usually has robust performance in most ML tasks
	Support vector classification (SVC)	Classification	
Gaussian process (GP)[180,181]	Gaussian process regression (GPR)	Regression	GP develops from Bayesian theorem, and has few parameters to be adjusted
	Gaussian process classification (GPC)	Classification	
Deep learning	Artificial neural networks (ANN)	Regression and classification	Composed of dense layers
			Suitable for 2-dimensional data
	Convolutional neural network (CNN)	Regression and classification	Used for image data
	Graph convolutional neural network (GCNN)[38]	Regression and classification	Used for coordinates data
	Recurrent neural network (RNN)[184]	Regression and classification	Used for sequential data
	Long short-term memory (LSTM) network[184]	Regression and classification	Used for sequential data
	Gate recurrent unit network[184]	Regression and classification	Used for sequential data
	Generative adversarial network (GAN)[185–187]	Regression and classification	Consist of an unsupervised *generator* model and a supervised *discriminator* model, aiming to produce promising candidates for inverse design
	Variational autoencoder (VAE)[188]	Regression and classification	Involve an *encoder* network and a *decoder* network, and build latent space to represent material structures

Ensemble methods

Ensemble methods have gained significant popularity in recent years due to their merits of robustness, stability, and generalization[38,166], which particularly refers to the tree-based mathematic approaches of assembling multiple CART models to promote the performance over a singular tree model.

Averaging approach. One common case in ensemble methods is the averaging approach, which leverages the outputs from the several parallelly and independently fitted CART models on average. The base models might be trained on different training sets that are sampled from the whole dataset. When the random sample subsets are drawn for each CART model, the algorithm is called pasting[167]. When the random sample or feature subsets are drawn with replacement, the method is known as bagging[168] or random subspaces[169]. If the random sample and feature subsets are both drawn with replacement, the method is entitled RF[170]. The base models are organized together and make a collective decision, in which the sklearn package provides the basic module "Voting Class" that is convenient to fill any other model rather than the CART model. Takahashi *et al.* trained a RF model to predict bandgaps of perovskite materials and estimated 9328 candidates, where 11 undiscovered Li-/Na-based structures had an ideal bandgap and formation energy for solar cell applications[171].

Boosting approach. Another case in ensemble methods is the boosting approach. The critical idea here is to build a series of CART models in sequence, with each model fitted to reduce the whole bias from the former assembled CART models. The final outputs of the boosting model are then determined by the whole sequentially fitted CART models. Adaboost was the first proposed boosting algorithm whose trait is to repeatedly modify the sample weights in each step of building a new CART model, in which the weights of the samples with large predicted errors are enhanced and each new CART model is trained on the reweighted samples[172]. The most prevailing algorithm under the boosting theory is GBM and its derivatives, also known as gradient boosting trees (GBTs)[173]. Rather than modifying sample weights, each CART model in GBM is trained to predict the bias resulted from the whole former models and the finial outputs are the sum of the whole model predictions. The derivatives aim to reduce the computing cost and promote the fitness of GBM. XGBoost is proposed by imposing a second-order Taylor approximation and L2 regularization into the loss function, which can simplify the procedure of building each CART model[50]. The light gradient boosting machine (LightGBM) introduces gradient-based one-side sampling and exclusive feature bundling to largely reduce the sample numbers and the feature dimensions to lower the computing and memory costs when dealing with gigantic data[174]. CatBoost adopts an ordering principle to handle the specified cases that contain a large number of categorical features[51,175]. Sahu *et al.* employed RF and GBM models to predict the OSC device performance based on 13 material descriptors, giving the similar cross-validation results for PCE values with R^2 values of 0.78 for GBT and 0.76 for RF[176].

Support vector machine

SVMs, including support vector classification (SVC) and support vector regression (SVR), are also some of the most widely-used algorithms and have become a must-try method because of their robust performance and fast computing efficiency[48,177,178]. With a kernel function, SVC finds a separating hyperplane with the maximum margin in a high-dimensional space, while SVR regresses responses and features in a high-dimensional space and tolerates error ε on each side of the fitting hyperplane. In the work of Wu *et al.*, the SVR model was fitted to predict the unit cell volume of HOIPs for photovoltaic systems, with an R^2 value of 0.989[179].

Gaussian processes

Gaussian processes (GPs) for ML are developed based on the Bayesian theorem and Gaussian probability distribution[180,181]. Unlike in other deterministic ML regressions, GP regression utilizes the Gaussian probability distribution to regress data and express regression results in terms of mean and covariance of the maximal posterior distribution. The following are the responses $\boldsymbol{y}$ used in training and the responses $\boldsymbol{y}_*$ to be predicted to form a joint normal distribution of $\begin{pmatrix} \boldsymbol{y} \\ \boldsymbol{y}_* \end{pmatrix}$ with a zero mean and joint covariance:

$$p\begin{pmatrix} \boldsymbol{y} \\ \boldsymbol{y}_* \end{pmatrix} \sim N\left(\begin{pmatrix} 0 \\ 0 \end{pmatrix}, \begin{bmatrix} \boldsymbol{K} & \boldsymbol{K}_*^T \\ \boldsymbol{K}_* & \boldsymbol{K}_{**} \end{bmatrix}\right) \tag{7}$$

where $\boldsymbol{K}$ and $\boldsymbol{K}_{**}$ are the covariance matrixes for data $\boldsymbol{X}$ and $\boldsymbol{X}_*$, respectively, and $\boldsymbol{K}_*$ is the covariance correlated between data $\boldsymbol{X}$ and $\boldsymbol{X}_*$. The joint distribution is expressed by:

$$p\begin{pmatrix} \boldsymbol{y} \\ \boldsymbol{y}_* \end{pmatrix} = p\left(\boldsymbol{y}_*|\boldsymbol{y}\right) p(\boldsymbol{y}) \tag{8}$$

Clearly, the predication of $p(\boldsymbol{y}_*|\boldsymbol{y})$ is also a conditional normal distribution:

$$p\left(\boldsymbol{y}_*|\boldsymbol{y}\right) = \frac{p\begin{pmatrix} \boldsymbol{y} \\ \boldsymbol{y}_* \end{pmatrix}}{p(\boldsymbol{y})} \tag{9}$$

The prediction follows the normal distribution $p(\boldsymbol{y}_*|\boldsymbol{y}) \sim N(\boldsymbol{K}_*\boldsymbol{K}^{-1}\boldsymbol{y}, \boldsymbol{K}_{**} - K_*\boldsymbol{K}^{-1}\boldsymbol{K}_*^T)$. The covariance matrix $\boldsymbol{K}$ is calculated by a kernel function. For example, the radial basis function in Equation (3) is the common choice to solve non-linear problems:

$$k_{ij}\left(\boldsymbol{x}_i, \boldsymbol{x}_j\right) = \exp\left(-\frac{1}{2}\left|\frac{\boldsymbol{x}_i - \boldsymbol{x}_j}{l}\right|^2\right) \tag{10}$$

where $k_{ij}(\boldsymbol{x}_i, \boldsymbol{x}_j)$ represents the element value in covariance matrixes and l is a parameter. The GP models were successfully fitted to predict the PCE values for organic photovoltaic materials[68,182].

Deep learning

Artificial neural network. The term deep learning (DL) refers to miscellaneous architectures of neural networks. The artificial neural network (ANN) or multi-layer perceptron has the simplest and most understandable structure, whose structural units comprise the fully connected layers (known as dense layers). As shown in Figure 3A, a deep ANN model is composed of multiple dense layers with a conic distribution in layer length. The input data, starting from the input layer, are processed through all the dense layers by multiplying each parametric weight matrix in each layer, which is finally output as the predicted value. A typical example can be found in the work of Li *et al.*, in which the trained ANN model for PSCs achieved the best performance against the other ML models with the highest R^2 value of 0.97 for bandgap predictions and the highest value of 0.80 for PCE predictions[183].

Convolutional neural network. By appending convolution layers in front of the dense structure, as shown in Figure 3B, the convolutional neural network (CNN) is formed to extract spatial features from images, which can be applied in processing characteristic results that are presented as images, such as from XRD, XPS, and so on[38]. As mentioned in the descriptor section, the GCNN is suitable for convolving spatial structure information from coordinate data and has been applied in predicting the moduli, formation energy, and bandgap of crystal structures from the Materials Project[52] by Xie *et al.*[120].

Recurrent neural network. Other advanced DL architectures may also have significant potential for materials science applications, though there have been few reported publications. For example, when dealing with sequential data, including various spectra data, the recurrent neural network (RNN), long short-term memory (LSTM) network, and gate recurrent unit network can be exerted to train the relevant model[184].

Generative adversarial network. The generative adversarial network (GAN)[185–187] is a sophisticated DL architecture consisting of an unsupervised *generator* model and a supervised *discriminator* model, which aims

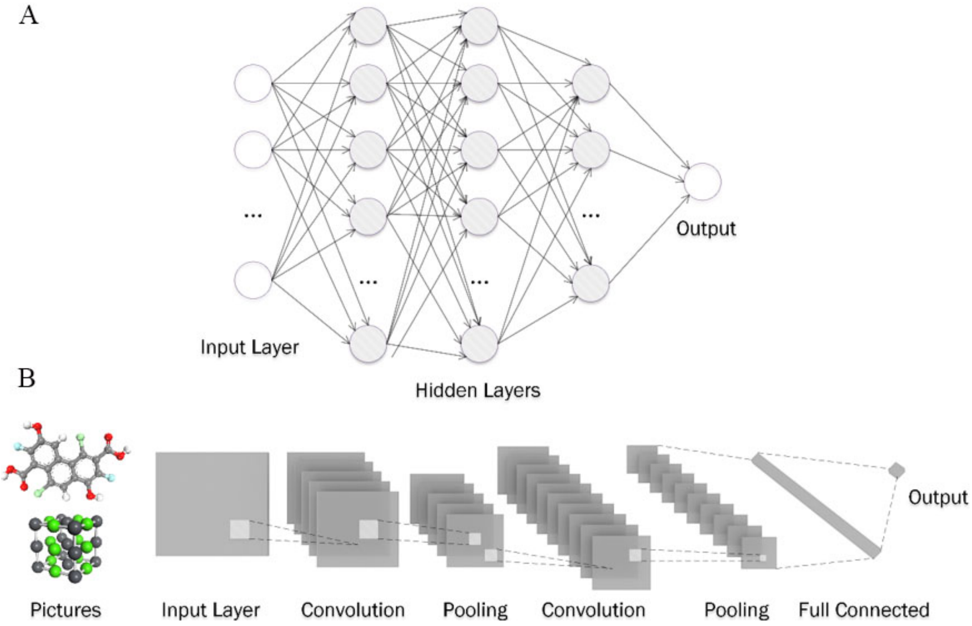

Figure 3. Architectures of (A) artificial and (B) convolutional networks.

to produce promising candidates for inverse design[184] Specifically, the goal of a *generator* model is to fit a function $p_{model}(\boldsymbol{x})$ that approximates the real sample distribution $p_{real}(\boldsymbol{x})$ with no direct access to real data points. The *discriminator* model has access to both the real and fake samples (drawn from the *generator* model), whose purpose is to differentiate from the real or fake. The error via the *discriminator* model can be used to train both the *discriminator* and *generator* models. Given a well-trained GAN model, we may use the *generator* model to design reliable candidate structures without human intuition. Though the applications of the GAN model are largely restrained because of the difficulties in converging the pair of models and the need for a significant amount of real data samples of high quality[185–187], we expect that these bottlenecks will be overcome as data samples accumulate and the GAN develops.

Variational autoencoder. The variational autoencoder (VAE)[188] is a comparable DL architecture to GAN involving an *encoder* network and a *decoder* network, whose novelty is to build a so-called latent space to represent the material structures[63] Crucially, the *encoder* network maps the material structures (in the SMILE or CIF format) to vectors in a lower-dimensional space known as latent space, which acts to compress the information from the original data into the vector in latent space. Furthermore, the *decoder* network performs the inverse operations to decompress the vector to its original form. By training both the *encoder* and *decoder* networks to process and reproduce the original data, the VAE model is expected to learn the potential features from the real data samples. Benefitting from the continuous and differentiable vectors in latent space, we can extrapolate and construct new reliable material structures by applying direct search engines (e.g., greedy search), since latent space is a continuous vector space.

Evaluation metrics

Before an ML/DL model is trained, as discussed in section ”Data preprocessing” (section 2.3) , a dataset is usually divided into a training set, validating set, and test set. The prediction of a trained model on the training set is referred to as the training prediction and the relevant metrics are known as the training metrics. The training metrics usually reveal good performance since the samples are already used in training and therefore cannot be an effective indicator for the model performance. Similarly, the validating and test predictions and metrics can be obtained when predicting the samples in the validating and test sets. Good validating metrics are adopted to optimize the hyperparameters, if any. High performance in test metrics signifies excellent predictivity and generalization abilities.

In regression, the determination coefficient (R^2), as seen in the previous examples, is the most critical and common indicator for model performance, in which a higher value signals better model performance. Given an observation y_i of sample i, the corresponding prediction $\tilde{y}_i$, and the mean value of the observations $\bar{y}$, R^2 is defined as:

$$R^2 = 1 - \frac{\sum (y_i - \tilde{y}_i)^2}{\sum (y_i - \bar{y})^2} \tag{11}$$

The Pearson correlation coefficient (ρ) is also often employed in regression and in the correlation examination of features. Given the observation (or feature) $\boldsymbol{y}$, prediction (or another feature) $\tilde{\boldsymbol{y}}$, their covariance array $cov(\boldsymbol{y}, \tilde{\boldsymbol{y}})$ and their standard deviations σ, ρ is defined as:

$$\rho = \frac{cov(\boldsymbol{y}, \tilde{\boldsymbol{y}})}{\sigma_{\boldsymbol{y}} \sigma_{\tilde{\boldsymbol{y}}}} \tag{12}$$

The values of ρ range from -1 to 1. The maximum 1 reveals a perfectly positive linear proportion relation and the minimum -1 shows a perfectly negative linear proportion relation.

Various prediction errors can be adopted to signal the model predicting error. For example, the mean absolute error (MAE) is the mean of the absolute difference between each observation and prediction. The mean squared error (MSE) is calculated from the mean of the squared difference. The root mean squaref are the correctly predicted while the off-diagonal elemen error (RMSE) is the root of the MSE. The value ranges of error metrics are largely dependent on the target range.

In the classification task, the total accuracy can be used to indicate the performance of classification models, which is the division between the correctly predicted samples and the whole samples. To gain more detail, the confusion matrix, also known as the error matrix, can be employed, which is an N-square array (N is the categorical number of labels), as shown in Figure 4A. The columns represent the observed labels and the rows indicate the predicted labels (the definitions of the two axes can be swapped). The element in each pixel expresses how many samples belonging to the observed label are estimated as the predicted label. Apparently, the diagonal elements are correctly predicted, while the off-diagonal elements are all incorrect. The accuracies of a specified class can be obtained by dividing the specified diagonal element by the sum of the corresponding row. With regards to the binary classification that contains the positive or negative labels, as shown in Figure 4B, the correctly predicted positive samples are deemed true positive (TP), while the correctly predicted negative, incorrectly predicted positive and incorrectly predicted negative samples are referred as true negative (TN), false positive (FP), and false negative (FN), respectively. *Precision* is defined as the accuracy of the positive samples, while the *recall* score refers to the division of TP over the sum of TP and FP, representing the ability of the classification to find the positive samples with the best value of 1. The F1 score is the combination of the *precision* and *recall* score, defined as:

$$F1 = \frac{2 \times (precision \times recall)}{precision + recall} \tag{13}$$

The F1 score is interpreted as a weighted average of the precision and recall score, whose best value reaches 1 and the worst is 0.

In a clustering task, the Silhouette coefficient (SC) is the most common indicator, which is calculated as[189]:

$$SC = \frac{1}{N} \sum_{i=1}^{N} \frac{b_i - a_i}{\max (a_i, b_i)} \tag{14}$$

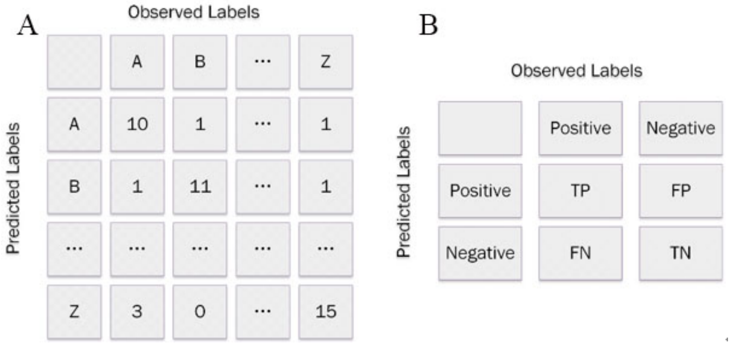

	A	B	···	Z
A	10	1	···	1
B	1	11	···	1
···	···	···	···	···
Z	3	0	···	15

	Positive	Negative
Positive	TP	FP
Negative	FN	TN

Figure 4. Classification task for (a) multiple and (b) binary labels. TP: True positive; TN : true negative; FP: false positive; FN: false negative.

where a_i is the mean distance between the sample i and all other points in the same cluster, b_i is similar to parameter a_i but differs in the next nearest cluster and N is the sample number. A higher SC value indicates better performance of a cluster model, namely, the overlapping areas among clusters are close to zero.

Hyperparameter optimization

Each algorithm might have its own hyperparameters that cannot be directly trained in the training process, such as a penalty factor, kernel function for SVM, CART tree number, learning rate for GBM, and so on. The hyperparameters need to be optimized to gain the best set of hyperparameters for a specified model. The grid search (GS) approach combined with K-CV is the most common method, and it exhaustively exploits the whole hyperparameter search space to find the globally optimal parameter set, which is effective for a discrete search space consisting of only a few hyperparameters but is unacceptable regarding time and computational cost for a uniform search space with multiple dimensions. Due to its simplicity, GS has been widely employed in current publications. Hartono *et al.* optimized the KNN, RF, GBM, ANN, and SVM models using the GS approach from the sklearn package[81], while Choudhary *et al.* utilized the same method to exploit the hyperparameters for the LightGBM model[190].

To overcome the high expense of the GS approach regarding time and computational cost, various alternatives have been proposed. The sequential model-based optimization (SMBO) constructs a surrogate model to approximate the hyperparameter distribution in the hyperparameter space. In SMBO, the hyperparameters and optimized object (e.g., LOO RMSE or CV5 MSE of the ML model) are regarded as the input and output, respectively. The criterion of *expected improvement (EI)* is usually adopted as the optimized object in the SMBO method, which can be defined as Equation (15):

$$EI_{n^*}(\boldsymbol{m}) = \int_{-\infty}^{\infty} \max\,(n^* - n, 0)\; p(n|\boldsymbol{m})dn \tag{15}$$

where $\boldsymbol{m}$ is the one set of hyperparameters, n is the corresponding fitness value in model performance, n^* is set as a threshold of n and $p(n|\boldsymbol{m})$ is the probability distribution of n at the conditions of $\boldsymbol{m}$. Gaussian process regression (GPR) is usually recognized as a good choice for the surrogate model to approximate $p(n|\boldsymbol{m})$ because of its few parameters necessary to be optimized. Therefore, the SMBO method, combined with EI and GPR, is depicted as follows:

(1) Draw several random points $(\boldsymbol{m}, n)$ and set n^* as the best fitness value.
(2) Fit a GPR surrogate model to approximate $p(n|\boldsymbol{m})$.
(3) Find and evaluate several sets of optimal hyperparameters in current distribution $p_{model}(n|\boldsymbol{m})$ that maximizes $EI_{n^*}(\boldsymbol{m})$.
(4) Add the pairs of new evaluated points $(\boldsymbol{m}, n)$ to update the GPR surrogate model.
(5) Repeat steps 3 and 4 until the iteration terminates.

Bergstra *et al.*[191] proposed a tree-structured Parzen estimator approach to modify the EI criterion in the SMBO method, in which this strategy approximates $p(\boldsymbol{m}|n)$ and $p(n)$ instead of $p(n|\boldsymbol{m})$. $p(\boldsymbol{m}|n)$ is defined using two hyperparameter densities as Equation (16):

$$p(\boldsymbol{m}|n) = \begin{cases} l(\boldsymbol{m})\ if\ n < n^* \\ g(\boldsymbol{m})\ if\ n \geq n^* \end{cases} \tag{16}$$

where $l(\boldsymbol{m})$ is the density of the hyperparameter points whose corresponding fitness values are lower than the threshold n^* and $g(\boldsymbol{m})$ is the opposite. The threshold n^* is set to be some quantile γ (*e.g.*, one quantile, 25%) of the observed n values, and therefore $p(n < n^*) = \gamma$. Equation (15) can then be transformed as follows:

$$\int_{-\infty}^{n^*} (n^* - n) \frac{p(\boldsymbol{m}|n)p(n)}{p(\boldsymbol{m})} dn \tag{17}$$

By applying $p(n < n^*) = \gamma$, Equation (18) is reached:

$$EI_{n^*}(\boldsymbol{m}) = \frac{\gamma n^* l(\boldsymbol{m}) - l(\boldsymbol{m}) \int_{-\infty}^{n^*} p(n)dn}{\gamma l(\boldsymbol{m}) + (1-\gamma) g(\boldsymbol{m})} \propto \left(\gamma + \frac{g(\boldsymbol{m})}{l(\boldsymbol{m})}(1-\gamma)\right)^{-1} \tag{18}$$

Equation (18) shows that to maximize $EI_{n^*}(\boldsymbol{m})$, the favorable hyperparameter points should have the high probability under $l(\boldsymbol{m})$ and the low probability under $g(\boldsymbol{m})$ in pursuit of a lower $\frac{g(\boldsymbol{m})}{l(\boldsymbol{m})}$ and hence higher $EI_{n^*}(\boldsymbol{m})$.

Other useful methods may also have their own merits of automated searching, efficiency, and easy parallelization, such as the Optuna[192] and Ray[193] packages; however, they are beyond the scope of this review.

ML model applications combined with domain knowledge

High-throughput screening

Among the common ML model applications listed in Table 4, high-throughput screening might be the most popular method to apply a fitted model in materials science, which filters potential materials with the required properties that are predicted by the model. To decrease incorrect trials in experiments and accelerate the search procedure more efficiently, domain knowledge may be required not only to restrain the search space for candidate materials as much as possible in pursuit of low costs in time and computation, but also to downselect the optimal candidates from the high-throughput screening results.

Wu *et al.* prepared a search space of 230808 ABX_3 HOIPs constructed by 21 experimental organic cations for the A site, 50 metallic cations for the B site, and ten anions for the X site[179]. After the procedures of charge neutrality and stability screening, the target bandgaps of the remaining 38086 HOIPs were predicted by the fitted GBM, SVR, and KRR models. Under the criterion of a bandgap range of 1.5-3.0 eV, 686 candidates were finally screened out.

Lu *et al.*[194] collected 1102 ferroelectric photovoltaic materials (407 perovskites and 702 non-perovskites) from the literature[195,196] to build up a classification GBM model to determine the perovskite structure and two regression GBM models to predict the bandgap and polarizability. The search space for the candidates was constructed by the elements involved in the dataset, leading to 19841 potential compounds in total. After being predicted by the three GBM models, 151 ferroelectric photovoltaic perovskites were shortlisted and further evaluated by first-principle calculations.

Gómez-Bombarelli *et al.* created a search space of over 1.6 million structures to identify promising novel organic light-emitting diode (LED) molecules[197]. An ANN model was trained to predict the delayed fluorescence rate constant. A total of 2500 candidates were filtered with suitable predicted values and further evaluated by human experts on a custom web voting tool. The four best potential candidates voted by the

Table 4. Popular ML model applications

ML model application	Description	Examples
High-throughput screening	Use a well-fitted model to predict huge potential materials generated from permutations. The materials are furtherly filtered by domain knowledge and the optimal candidates are down-selected from the large-scale samples.	Wu *et al*. predicted the bandgaps of 38086 HOIPs using GBM, SVR, and KRR models.686 candidates with bandgaps of 1.5-3.0 eV were selected [179]
		Lu *et al*. used three GBM models to predict the structure type, bandgaps and polarizabilities of 19841 ferroelectric photovoltaic materials, resulting in 151 shortlisted candidates [194]
		Gómez-Bombarelli *et al*. built an ANN model to predict the delayed fluorescence rate constant of 1.6 million LED molecules, leading to the four most promising ones that were further identified by experiments [197]
Online ML model	The fitted models could be shared to other researchers on websites. The visitors could obtain the predictions from the online models directly by uploading their own data as the required format.	Lu *et al*. [93] provided two BODIPY dye models to predict the PCEs at http://materials-data-mining.com/bodipy/
		Tao *et al*. [198] offered one model to predict the bandgaps of perovskite oxides at http://materials-data-mining.com/ocpmdm/material_api/ahfga3d9puqlknig and another model to predict corresponding hydrogen production at http://materials-data-mining.com/ocpmdm/material_api/i0ucuyn3wsd14940
		Xu *et al*. [199] afforded their model to predict polymer bandgaps at http://materials-data-mining.com/polymer2019/
Model analysis	Critical factors could be identified by calculating feature importance and further analysis to explore the underlying principles between properties and structures.	Xiong *et al*. [39] identified the vital features $\overline{VEC}$, H_{mix}, δ_{XP}, and δ_{Tb} for the hardness and UST of CCAs by analyzing RF models
		Zhang *et al*. extracted the important features from XGBoost model, including the radius, first ionization and lattice constant of B site, the radius of A site and tolerant factor [143]
		Jin *et al*. pinpointed the most crucial feature packing factor from GBM model [200]
		Yu *et al*. [157] obtained the significant features of sigma orbital electronegativity, acceptor site count, Balaban index, donor count and distance degree from lasso model

ML: Machine learning; GBM: gradient boosting machine; SVR: support vector regression; KRR: kernel ridge regression; ANN: artificial neural network; LED: light-emitting diode; BODIPY: boron-dipyrromethene; PCE: power convention efficiency; $\overline{VEC}$: valence electron; H_{mix}: mixing enthalpy; δ_{XP}: the mismatch in elemental first ionization potentials; δ_{Tb}: the mismatch in elemental boiling points; UST: ultimate tensile strength; CCAs: complex concentrated alloys.

experts were finally synthesized and tested experimentally, with a consistent result with the model predictions found with a mean unsigned error of 0.1 μs^{-1}.

Online ML models

Fitted models can be shared with other researchers by providing them on public websites, and this is an area where significant progress has been achieved in our group. For example, two boron-dipyrromethene (BODIPY) dye models were provided at http://materials-data-mining.com/bodipy/, which are widely accessible to use as established models for predicting the PCE values of BODIPY devices [93]. Tao *et al*. constructed two models for predicting the bandgap (http://materials-data-mining.com/ocpmdm/material_api/ahfga3d9puqlknig) and hydrogen production rate (http://materials-data-mining.com/ocpmdm/material_api/i0ucuyn3wsd14940) of perovskite oxides [198]. It is only required for the users to provide chemical formulas to predict the bandgap and formulas plus experimental conditions to predict the hydrogen production rate. Xu *et al*. afforded their model to predict the bandgap of polymers at http://materials-data-mining.com/polymer2019/, along with a full illustration of the ML training procedure [199].

Model analysis

In addition to models predicting applications, analysis based on feature importance can also help to identify critical factors, which can further clarify the underlying principles between the factors and properties by combining our domain knowledge. The SHAP approach is one emerging method for the analysis of feature contributions to model predictions.

In one of our recent works[39], SHAP was employed to explore the feature importance in established RF models that were targeted to hardness and ultimate tensile strength (UTS) for complex concentrated alloys (CCAs), in which the most vital features were identified, covering the valence electron $\overline{VEC}$, the mixing enthalpy H_{mix}, the mismatch in elemental first ionization potentials δ_{XP} for the hardness and the mismatch in elemental boiling points δ_{Tb}, H_{mix} for UTS. Specifically, the features $\overline{VEC} < 7.67$, $H_{mix} < -9.8$ KJ/mol, $\delta_{XP} > 0.067$ for the hardness and $\delta_{Tb} > 0.15$ and $H_{mix} < -14.6$ KJ/mol for UTS resulted in positive Shapley values that contributed to larger predictions.

We also applied SHAP to identify the most important structural factors to predict the formability of HOIP materials[143], in which the XGBoost classification model was built based on 102 HOIP samples and the filtered atomic descriptors along with the LOOCV accuracy of 95% and test accuracy of 88%. According to the SHAP analysis, it was found that the radius and lattice constant of the B site in ABX_3 were positively related to the formability, while the A site radius, tolerance factor, and first ionization of the B site have negative relations. Given the established model, 198 non-toxic HOIP candidates with a probability of formability over 0.99 were screened from 18560 virtual samples.

In the research of Jin *et al*., the feature importance from the GBM model was utilized to pinpoint the most crucial feature known as the *packing factor*[200], while Yu *et al*. adopted the feature importance from the lasso model to identify the significant features of sigma orbital electronegativity, acceptor site count, Balaban index, donor count and distance degree[157].

RECENT PROGRESS OF DATA-DRIVEN METHODS

Data-driven progress in PSCs

As discussed in the introduction, despite innumerable merits as absorbers in solar cell devices, perovskite materials, especially in the case of HOIPs, still face imperfections regarding scalability, stability, and environmental pollution. Scalability is mostly related to deposition, film formation, and device integration[201,202], which are beyond the scope of this review. The remaining two issues are mainly attributable to the unstable structures and the incorporation of Pb in HOIPs, e.g., the mostly used $MAPbI_3$, formamidinium lead iodide ($FAPbI_3$), and their derivatives. Most ML/DL studies, accompanying experimental ones, exploit the leading-edge aspects of promoting stability, lowering the fractions of polluting elements as much as possible, or designing new potential material alternatives. The typical ML publications of PSCs are summarized in Table 5.

As light absorbers, the bandgap is one of the most important properties for HOIPs and can act as a simple and initial criterion to rapidly inspect potential candidates. In this context, Saidi *et al*. established a complex hierarchical convolutional neural network (HCNN) to predict the bandgaps of ABX_3 HOIP structures with the simple inputs of atomic descriptors[83]. A total of 380 different compositional ABX_3 HOIP structures (expanded to 862 permutations obtained via rearrangements of the tri-halide moiety) were generated by arranging Cs in addition to 18 organic ions at the A site, Pb or Sn at the B site, and three halogens (excluding fluorine) at the X site. Their bandgaps, lattice constants, and octahedral angles were calculated as the relevant concerned ML targets based on DFT, while the structural coordinates extracted from the relaxed structures were treated as the inputs for the ML models. Two convolutional neural network (CNN) models were initially trained to predict the lattice constants and octahedral angles with RMSE values of 0.01 Å and 40°, respectively. Therefore, an assembled HCNN model was formed by piping these two predicted properties as the partial features coupled with the structural coordinates to the third CNN model that was targeted towards bandgaps, which exhibited a low RMSE value of 0.02 eV. Considering the initial inputs and ultimate output, the model of Saidi successfully predicted the bandgap based on only the information of the atomic coordinates rather than any other complicated DFT calculations. Such work may help us to accelerate DFT calculations by predicting DFT properties via ML models. However, it might be more convincible if the constructed HCNN model can

Table 5. Typical ML publications of PSCs

Publication	Sample	Feature	ML Task	ML Algorithm	(Best) Model Performance
Saidi *et al.*[83]	380 simulated ABX_3 HOIPs	Structural coordinates, lattice constants and octahedral angles	Predict bandgap	HCNN	RMSE 0.02 eV
Li *et al.*[101]	ABO_3 perovskite materials from Materials Project (758) and OQMD (1641)	66 descriptors generated from pymatgen package, and BVVS descriptor	Predict bandgap	SVM, RF, Bagging, GBT (best)	Test R^2 0.86
Jin *et al.*[200]	98 experimentally reported PV and 98 non-PV materials	22 structural descriptors	Identify photovoltaic materials or not	GBT (best), SVM, RF, Adaboost, SGDC, CART, and LR	Accuracy 100%
Zhao *et al.*[84]	Synthesized 1400 perovskite samples	A-site ion, stoichiometry, coating methods, aging temperatures, humidity, and illumination	Predict T_{80}	GBT (best), LR, and RF	CV RMSE 169
Hartono *et al.*[81]	Synthesized 260 CL samples for $MAPbI_3$	12 processing conditions and structural properties generated from PubChem database	Predict a key descriptor onset representing PSC stability	LR, KNN, RF (best), GBT, ANN, and SVM	CV RMSE 70.8
Zhou *et al.*[203]	9000 *ab initio* MD trajectories	Static and dynamic variables: 414 for 48-atom system, and 5440 for 384-atom system	Predict NAC and bandgap	KNN	
Lu *et al.*[224]	539 HOIPs and 24 non-HOIPs from reported experiments	Elemental/organic properties and structural factors	Determine formability	CatBoost	LOOCV and test accuracies 100%
Zhang *et al.*[143]	44 HOIs and 58 non-HOIPs from reported DFT calculations	Elemental/organic properties and structural factors	Determine formability (DFT)	XGBoost	LOOCV and test accuracies 91%-94%
Im *et al.*[225]	540 simulated double halide perovskites	32 features about atomic constituents and geometric information	Predict formation heat and bandgap	GBRT	Test RMSEs 0.021-0.223 eV
Li *et al.*[183]	333 reported perovskite samples	Material compositions	Predict bandgap and PCE	LR, KNN, SVR, RF, ANN (best)	Test ρ 0.72-0.97
Lu *et al.*[194]	1109 perovskites/non-perovskites from reported first-principles calculations	Elemental and material properties	Predict formability, polar structure, bandgap	GBM	Accuracy 89% R^2 0.916-0.921
Sun *et al.*[226]	Fabricated 75 perovskite films	XRD and absorption data	Classify 0D, 2D and 3D structures	ANN	Accuracy 90%
Wu *et al.*[179]	1346 simulated HOIPs	32 elemental properties and structural factors	Predict bandgap	GBR (best), SVR, KRR	R^2 0.827
Yu *et al.*[157]	Synthesized 50 amines for post-treatment	Organic descriptors	Determine whether perovskite films are destroyed after post-treatment	LR, SVM (best), KNN, decision tree, Gaussian Naive Bayes	Test accuracy 86%
Lu *et al.*[227]	346 HOIPs from reported first-principles calculations	30 elemental and structural features	Predict bandgap	GBR (best), KRR, SVM, GPR, decision tree, ANN	Test R^2 0.97
Li *et al.*[228]	354 simulated halide perovskites	Elemental and structural features	Predict decomposition energy	KRR, KNN, SVR	RMSE 42-54 meV
Schmidt *et al.*[229]	250000 simulated cubic perovskite materials	Elemental and structural features	Predict thermodynamic stability	RR, RF, extremely randomized tree, Adaboost (best), ANN	Test MAE 121.3 meV/atom

ML: Machine learning; PSCs: perovskite solar cells; ABX_3: the perovskite materials formulated as ABX_3; HOIPs: hybrid organic-inorganic perovskites; DFT: density functional theory; HCNN: hierarchical convolutional neural network; RMSE: root mean squared error; ABO_3: the perovskite materials formulated as ABO_3; OQMD: open quantum materials database; BVVS: bond-valence vector sum; SVM: support vector machine; RF: random Forest; GBT: gradient boosting tree; R^2: determination coefficient; PV: photovoltaic; non-PV: non-Photovoltaic; SGDC: stochastic gradient descent classifier; CART: classification and regression tree; LR: linear regression; T_{80}: the time (in hours) required to decay 20% from PCE initial value; CV: cross-validation; CL: capping layer; $MAPbI_3$: methylammonium lead iodide; PubChem: A database: https://pubchem.ncbi.nlm.nih.gov/; KNN: K-nearest neighbor; NAC: nonadiabatic coupling; GBRT: Gradient boosting regression tree, the same as GBT or GBM; GBM: Gradient boosting machine; 0/2/3D - 0/2/3-dimensional; GPR: gaussian process regression; RR: ridge regression; MAE: mean average error; CatBoost: A new boosting approach of ensemble method: https://catboost.ai/; XGBoost: A new boosting approach of ensemble method: https://xgboost.readthedocs.io/

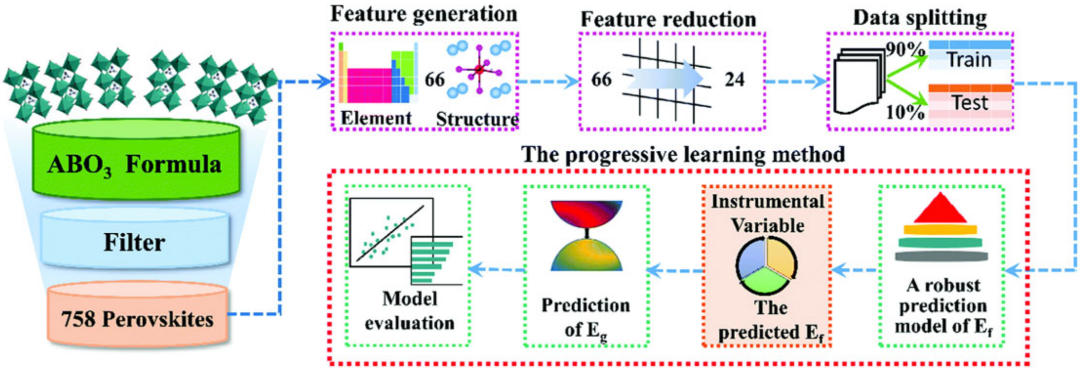

Figure 5. Overall workflow of progressive learning method. The schematic presents the details of a collection of perovskites and the outlines of a progressive learning workflow, including instrumental variable generation, bandgap (E_g) prediction, and results analysis. Reproduced with permission from Li *et al*., J. Mater. Chem. C **8**, 3127 (2020). Copyright 2020 Royal Society of Chemistry[101].

be validated by some external samples to show the generalizability of the model available, since the overfitting problem is very common for CNN-like models.

Similar to the work of Saidi, Li *et al*. explored the chemical space of ABO_3 perovskite materials based on 758 samples distributed over seven kinds of phases with the relevant targeted bandgaps between 0 and 5 eV from the Materials Project as the training dataset and 1641 materials from OQMD as the validation dataset[101]. The overall workflow of this work can be seen in Figure 5. In total, 66 descriptors were mainly generated from the pymatgen package[102] in Python (labeled as basic descriptors), plus the so-called bond-valence vector sum (BVVS) descriptors, while four algorithms were used for the ML models, including the SVM, RF, bootstrap aggregating algorithm (Bagging) and GBT. Eight ML models targeting formation energies and bandgaps were established, with R^2 values for the validation dataset of 0.953, 0.949, 0.960, and 0.964 for the formation energies and 0.674, 0.808, 0.790, and 0.822 for the bandgaps, respectively. Similar to the strategy of Saidi, the prediction of formation energies was then treated as the additional input feature, together with the initial basic and BVVS descriptors (totaling 67), to further predict the bandgap, in which the remolded models, via four algorithms, gained R^2 values of 0.734, 0.821, 0.800, and 0.855, respectively. Finally, a feature selection known as "last-place elimination" based on the GBT model was performed, resulting in an optimal set of 26 features and promoted R^2 values of 0.760, 0.813, 0.817, and 0.856, respectively. The contributions of 26 selected features were ranked by the GBT algorithm, and it was found that the electron number of the d orbital played the most important role, followed by the predicted formation energies. The BVVS on the O site also had a significant contribution, which was chosen to characterize the distortion of the BO6 octahedron. A relatively simple GBT model was built to predict the quantum-based bandgaps of ABO_3 perovskite materials, which exhibited the reliable model generalizability on the validation set. The newly introduced descriptor BVVS revealed its distinct promotion for building ML models, which may inspire us to explore more informative descriptors for perovskite materials.

Compared to the discovery of potential materials by predicting suitable bandgaps, Jin *et al*. established a classification model to directly identify 2D photovoltaic materials[200]. To perform the classification task, they collected 98 experimentally reported photovoltaic and 98 non-photovoltaic materials, accompanied by the generation of 22 structural descriptors that were evaluated and ranked by their feature importance. The packing factor (P_f), average sublattice neighbor count, Mulliken electronegativity minimum value, and average atomic volume played the leading roles in identifying the PV candidates. The backward selection approach was then employed based on the ranked feature importance to exclude the features with minimal influence on photovoltaic properties, leaving 19 features reserved. Several ML algorithms were employed to construct the models, including the GBT, SVM, RF, Adaboost, stochastic gradient descent classifier (SGDC), CART, and LR. GBT gained the best accuracy, recall, and precision scores (all 100%), while the others performed at ~90%. A total of 3011 PV candidates from 187093 unexplored materials in the ICSD were identified by the GBT model. It is noteworthy that the P_f values of these candidates were concentrated between 0.3 and 0.5, and the candidates with the P_f value particularly fixed at 0.33 had a 30% chance of being PV materials. The authors further filtered 26 materials using a criterion known as dimensionality and computed the theoretical PCE-based DFT methods. As a result, three materials, i.e., Sb_2Se_2Te, Sb_2Te_3 and Bi_2Se_3, exhibited the highest theoretical PCEs. Taking the electronic properties of SB_2Se_2Te as an example, it was found that this outstanding performance might be related to the p-p optical transition in Sb_2Se_2Te enabled by the lone-pair s orbitals of Sb and the built-in electric field induced by the asymmetric geometry. Nevertheless, the further application of the constructed GBT model might be constrained due to the small size of the dataset. It, therefore, might be more reliable if the dataset is expanded or the model is validated by unknown samples or stability tests.

Furthermore, Zhao *et al.* combined a robotic system, ML, and experiments [Figure 6] to assess the photothermal stability of $APbI_3$ mixed cation perovskites under different aging conditions[84]. They fabricated over 1400 $APbI_3$ perovskite samples with 64 compositional combinations by varying the A-site ion (K, Rb, Cs, MA or FA), stoichiometry, coating method (drop or spin coating), aging temperature (60, 85, 100 or 140 °C), humidity (0% or 10%) and illumination (dark or light). The figure-of-merit, namely, the studied target, was denoted as T_{80}, which indicates the time (in hours) required to decay 20% from its initial value. The GBT algorithm was adopted to perform the model construction, with the lower test set RMSE value of 169 compared to the test set RMSEs for LR (651) and RF (527). SHAP combined with the GBT algorithm was used to interpret the feature importance at different aging temperatures. It was found that the over-stoichiometric condition (e.g., $K_{0.05}FAPbI_{3.05}$) led to worse stability caused by the higher defect density. The authors also discovered that the incorporation of Cs was beneficial to the stability of perovskites over 100 °C but detrimental under 100 °C, while the doping of MA was overall neutral for stabilizing perovskites and had a positive effect at low temperatures. Subsequently, the authors performed theoretical simulations to compare the energy costs of perovskite decomposition and the activation energies of possible decomposition pathways, resulting in the same conclusion that the incorporation of Cs in $FAPbI_3$ could increase the crystal formation energy and simultaneously decrease the gas desorption barrier, while MA exerts the opposite effects. Additionally, the authors fabricated $MA_xCs_{0.15-x}FA_{0.85}PbI_3$ with an n-i-p structure of ITO/(SnO_2:PEIE)/(PCBM:PMMA)/$MnSO_4$/perovskite/PDCBT/Ta-WOx/Au and the device containing the composition $MA_{0.1}Cs_{0.05}FA_{0.85}PbI_3$ maintained 90% of the peak PCE value after 1800 h of continuous operation, in which 10 mol.% organic MA and up to 5 mol.% inorganic Cs/Rb might be a promising incorporation strategy to improve the device stability at below 100 °C. This work excellently applied ML techniques to accelerate the experimental progress by analyzing the influence of vital experimental conditions based on the GBT model and SHAP method.

Considering that the addition of an inert capping layer (CL) might be beneficial to the stability of $MAPbI_3$, Hartono *et al.* considered 21 organic salts and 2 X-site anions (Cl/Br) to form potential CL candidates in order to identify whether the CL has the ability to enhance the stability of $MAPbI_3$ and to probe the underlying mechanisms[81]. For each CL film, 260 samples, along with their 12 processing conditions, were explored under the same aging test conditions (85% relevant humidity, 85 °C aging temperature and 0.16 Sun illumination). The authors photographed the samples every 3 min to record the color changes and defined a key descriptor

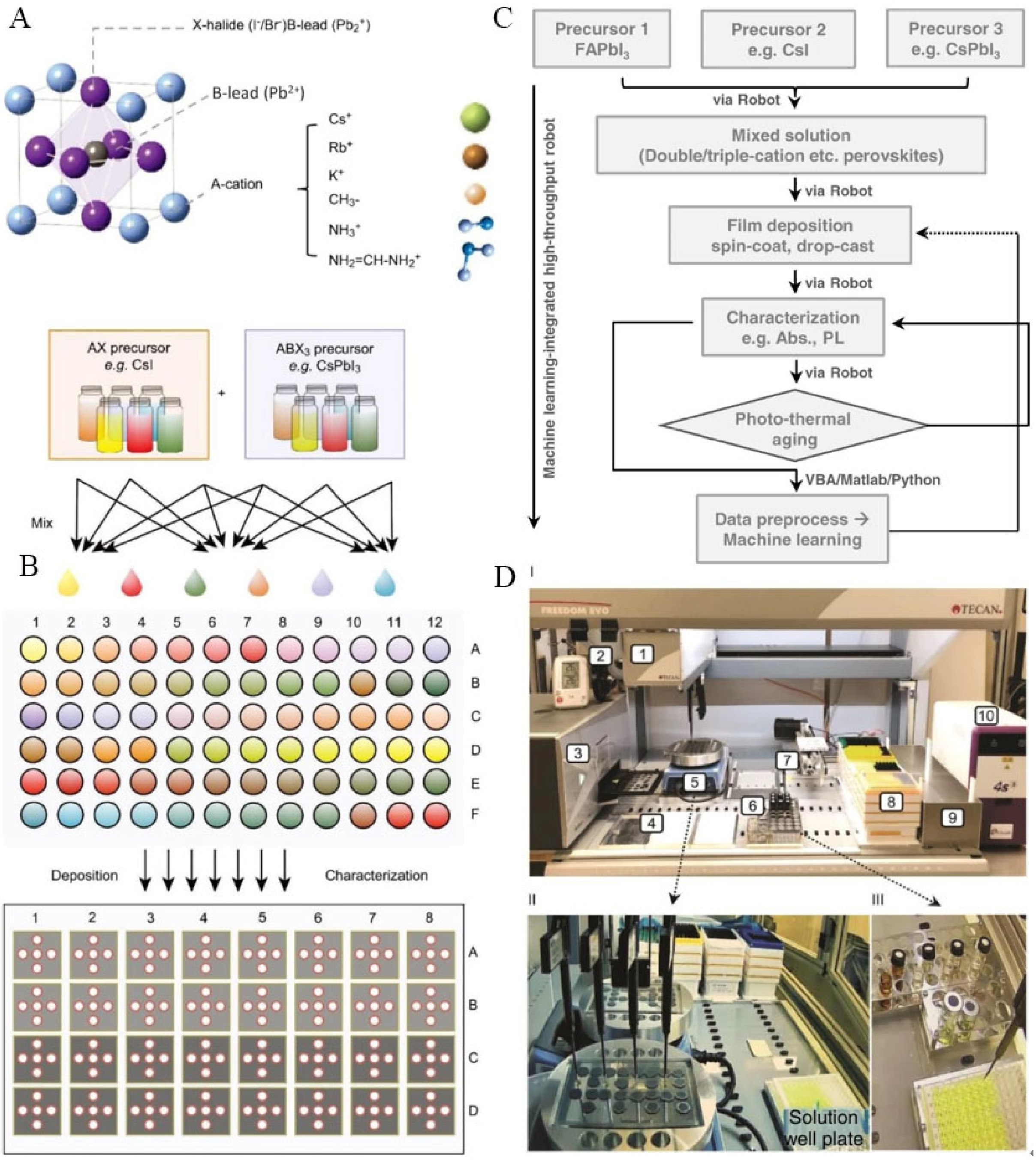

Figure 6. (A) Crystal structure of a perovskite with multiple cations, including potassium (K^+), rubidium (Rb^+), cesium (Cs^+), methylammonium (MA^+) and formamidinium (FA^+). (B) Schematic of HTRobot workflow for automatic synthesis and characterization. The red circles in the bottom panel indicate the five different positions tested on each sample. (C) Detailed workflow of high-throughput operation to evaluate perovskite stability. (D) Photograph of HTRobot system, including (1) a robot arm with four pipettes, (2) a camera and humidity meter, (3) a spectrometer to record the absorbance and photoluminescence, (4) 96-well microplates to mix the precursors, (5) a hotplate, (6) a stock solution of PbI_2, FAI, MAI, CsI and so on, (7) a sample stage, (8) pipette tips, (9) a waste container and (10) a heat sealer to optionally fuse microplates with aluminum foil. I, II, and III show a panoramic view of the setup and top views of the film fabrication and solution preparation, respectively. Reproduced with permission from Zhao *et al*.[84] Copyright 2021 Springer Nature.

onset for PSC stability as the time intercepts of the rapid color change from black to yellow. The onset was then labeled as the output of the ML models, while the 12 processing conditions were regarded as features coupled with the structural properties generated from the PubChem database, including molecular weight, partition coefficient, indicating the hydrophobicity/hydrophilicity of the molecules, rotatable bond number, complexity, topological polar surface area (TPSA), hydrogen-bond donor number and element numbers for C, H, Br, N and I. In total, six regression algorithms, namely, LR, KNN, RF, GBT, ANN, and SVM, were involved, in which the RF model gained the best RMSE value of 70.8. The RF algorithm was then combined with SHAP to interpret the model result, showing that the number of hydrogen-bond donors and TPSA were the most critical factors in determining the stability.

Motivated by the feature importance ranking, the authors further compared the top-performing CL material, namely, phenyltriethylammonium (PTEA), which had zero values for hydrogen-bond donors and TPSA, with other CLs via the methods of X-ray diffraction (XRD), scanning electron microscopy, grazing-incidence wide-angle-X-ray scattering and Fourier-transform infrared spectroscopy. The XRD data indicated that a new perovskite phase, $(PTEA)_2(MA)_3Pb_4I_{13}$, was formed on the top film of $MAPbI_3$. The other results revealed that the top-performing CL stabilized the $MAPbI_3$ perovskite by modifying the surface structure, coinciding with a suppression in the loss of methylammonium and the formation of both PbI_2 and oxygen-containing compounds at the surface of the perovskite. With the feature analysis via the RF model and SHAP method, the authors successfully discovered the vital features and identified PTEA as the most promising CL material. Combined with the results of the characterization, the new perovskite phase was recognized as the main factor influencing the device stability. Such work illustrates that ML technology can help us to find promising materials rapidly and reasonably and even reveal hidden principles.

In addition to materials discovery, ML has also been applied to quantum dynamics to help uncover complex mechanisms, such as charge carrier trapping in perovskites. For example, Zhou *et al*. employed the KNN algorithm to analyze the calculated results from *ab initio* nonadiabatic MD and the most important structural factors for the charge carrier dynamics and bandgap of $MAPbI_3$[203]. The work started from pristine tetragonal $MAPbI_3$ with a 48-atom 1 × 1 × 1 supercell and a larger 384-atom 2 × 2 × 2 supercell. A 9 ps *ab initio* MD trajectory for both of the two crystal structures was generated with a 1 fs time step. The nonadiabatic coupling (NAC, proportional to the charger carrier relaxation rate) and bandgap were calculated as the targeted properties for the crystal structure in each trajectory. A total of 414 structural and motional descriptors, including bond lengths/motions, bond angles/motions, dihedral angles/motions, crystal lattice motions, relative orientations, and distances, were generated for the 48-atom system, while 5440 descriptors were generated for the 384-atom system. The pairwise mutual information (MI) between each feature and target was estimated based on the KNN algorithm to reflect the correlations. The various angles/motions of I, Pb, and MA (especially the top three angles of I-I-I, I-Pb-I and Pb-I-Pb) shared the majority of the top highest MI values for both targets of the NAC and bandgap, while the crystal lattice motions showed much less importance than its internal bond and angle descriptors. These results reflected three conclusions: 1) the NAC values depended explicitly on nuclear velocity; 2) MA motions had a strong influence on the nonradiative relaxation since the MA motions shared one part of the top highest MI values; 3) the influence on nonradiative relaxation arose from the geometry of the Pb-I sublattice, mainly including I-I-I, I-Pb-I and Pb-I-Pb angles. The work of Zhou tended to explore the key factors that have impacts on the NAC and bandgaps of different $MAPbI_3$ structures instead of making model predictions directly. Such research might be more exhaustive if more model validations were accomplished.

Data-driven progress in DSSCs

One of the advantages of DSSCs is the mature process of their device fabrication due to decades of their development and optimization in experimental conditions. Most ML/DL efforts so far have focused on accelerating the discovery of new organic dye sensitizers with notable photovoltaic properties that are promising for leading performance in DSSC devices. The typical ML publications of DSSCs are summarized in Table 6.

Most recently, for the purpose of predicting the PCE values for DSSCs, Krishna *et al*. [Figure 7] prepared

Table 6. Typical ML publications of DSSCs

Publication	Sample	Feature	ML Task	ML Algorithm	(Best) Model Performance
Krishna *et al.*[90]	1200 reported dyes that could be divided into 7 chemical classes	Descriptors generated from Dragon 7 and PaDEL-descriptor software	Predict PCE	PLS	Test R^2 0.61~0.84
Wen *et al.*[141]	223 reported organic dyes	Descriptors extracted from DFT calculations	Predict PCE	GBT-SVM-ANN model with voting weight 4:7:4	CV5 ρ 0.76 Test ρ 0.78
Venkatraman *et al.*[207]	1961 reported organic dyes	Descriptors generated from ISIDA Fragmentor2017 and RDKit	Predict the natures of spectral shift	LDA, KNN, SVM, CART, RF (best), and GBT	Accuracy 71%~81%
Lu *et al.*[93]	58 reported BODIPY dyes	Descriptors generated from Dragon 7	Predict PCE	MLR	cLOOCV ρ 0.90~0.90 Test ρ 0.90~0.93
Cooper *et al.*[209]	9431 dye materials generated from ChemDataExtractor	Chemical structures, absorption wavelengths, and molar extinction coefficients	Discover new co-sensitizers	Text-mining method	
Kar *et al.*[89]	273 dye sensitizers	248 constitutional descriptors generated from Dragon 6	Predict PCE	MLR	Test R^2 0.60-0.97
Venkatraman *et al.*[230]	117 phenothiazine-based dye sensitizers	Molecular fragments	Predict PCE	PLS	Test R^2 0.68

ML: Machine learning; DSSCs: Dye-sensitized solar cells; Dragon 7: a software to generate organic descriptors: https://chm.kode-solutions.net/; PaDEL: a software to generate organic descriptors: http://www.yapcwsoft.com/dd/padeldescriptor/; PLS: partial least squares; R^2: determination coefficient; GBT: gradient Boosting Tree; SVM: support vector machine; ANN: artificial neural network; CV5: 5-fold Cross-validation; DFT: Density functional theory; ρ : pearson correlation coefficient; ISIDA Fragmentor2017: a software to generate organic descriptors: http://infochim.u-strasbg.fr/downloads/; RDKit: a software to generate organic descriptors: https://www.rdkit.org/docs/source/rdkit.Chem.EState.Fingerprinter.html; LDA: linear discriminant analysis; KNN: K-nearest neighbor; CART: classification and regression tree; RF: random Forest; BODIPY: boron-dipyrromethene; MLR: multiple linear regression; LOOCV: leaving-one-out Cross-validation; ChemDataExtractor: http://chemdataextractor.org/

the largest (till 2020) dataset composed of over 1200 dyes that could be divided into seven chemical classes to form the corresponding datasets, including 207 phenothiazines, 229 triphenylamines, 35 diphenylamines, 179 carbazoles, 58 coumarins, 281 porphyrins, and 158 indolines, which cover both metal-based and metal-free dye sensitizers[90]. The dye structures in the seven datasets were depicted by Dragon software version 7[86] and PaDEL-descriptor software version 2.21[91] to generate the descriptors based on their 2D dye structures, containing constitutional information, ring counts, connectivity index, functional group counts, atom centered fragments, atom type E-states, 2D atom pairs, molecular properties and extended topochemical atom indices. Each dataset was split into a training set and a test set using either the Kennard-Stone[204] or modified k-medoid method[205] in a ratio of 7:3. The descriptor pool was pre-treated to eliminate the intercorrelated descriptors, followed by feature selection using the in-house program "Best Subset selection v2.1 software". Seven descriptor sets were extracted from the feature selection, where 13 descriptors were selected for triphenylamines, 14 for phenothiazines, 13 for indolines, 12 for porphyrins, 5 for coumarins, 11 for carbazoles, and 4 for diphenylamines. For each training set, five statistically acceptable and robust individual models (IMs) were developed.

To enhance the prediction quality of the test set, the authors further used their in-house intelligent consensus predictor tool[153] to perform "intelligent" selection based on these five multiple PLS models to complement the shortages of any single model in their test set predictions. Therefore, four types of consensus models (CMs) were developed, in which CM0 referred to as the ordinary consensus model, CM1 leveraged the average of the predictions from the qualified IMs, CM2 was the weighted average predictions from the qualified IMs,

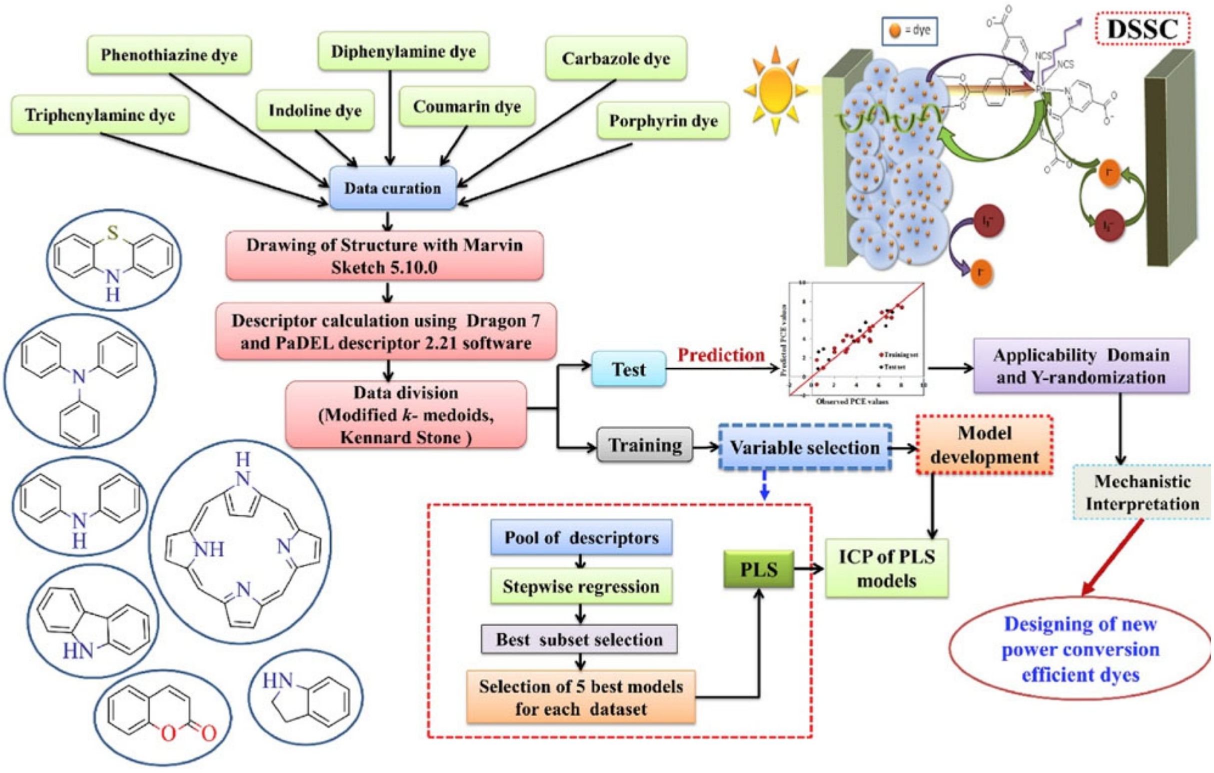

Figure 7. Schematic representation of the steps involved in the development of QSPR models. Reproduced with permission from Krishna *et al*.[90] Copyright 2020 Elsevier.

and CM3 signified the best model from the selected IMs. The CM3 model was the winning model for the triphenylamine, phenothiazine, indoline, and porphyrin datasets with determining coefficients R^2 on the test set of 0.61, 0.73, 0.74, and 0.69, respectively. Furthermore, for the carbazole and diphenylamine datasets, the four CM models had nearly the same performance, with R^2 values of 0.75 and 0.84. However, one model in the IMs shows the highest R^2 value of 0.68 for the case of the coumarin dataset rather than the CMs.

Afterwards, the authors discussed the mechanistic interpretations of all the descriptors obtained from the IMs for each dataset. For example, in total, ten descriptors appeared in the five IMs of the triphenylamine dataset, involving NdsN, B06[C-O], B07[O-S], B09[C-S], B06[O-S], C-038, C-043, nN(CO), EAT_Shape_Y, graph density, F05[N-N] and X4Av. NdsN represents the N atom numbers with double and single bonds (=N-), indicating the tendency of the localized π-π^* transition due to intramolecular charge transfer transition (ICT) from the triphenylamine donor, which showed a negative impact on the PCEs according to the negative variable coefficient in the IM equations. B06[C-O], B07[O-S], B09[C-S] and B06[O-S] denoted the presence/absence of C-O, O-S, C-S, and O-S atom pairs at the topological distances of 6, 7, 9 and 6 respectively. The presence of B06[C-O] led to the bathochromic shift of the absorption spectra and the enhancement of the molar extinction coefficient of the dye. B07[O-S] influenced the reduction of the absorption range and the shortening of rapid π-conjunction latency. B09[C-S] was related to the delocalization of the π electrons and the blue shift of the ICT band. C-038 represented the Al-C(=X)-Al fragment (Al referred to aliphatic groups and X referred to any electronegative atoms like O, N, S, P, Se and halogens), while C-043 represented the X-CR..X fragment (X refers to any group linked through carbon). Both of them had an impact on preventing the back-transfer of electrons from the conduction band of the semiconductor to the redox couple and thus reducing the charge recombination. The descriptor nN(CO) was the number of imides in the dye structures, which would improve the aggregation property of the dye over the TiO_2 surface and promote the recombination reaction between the redox electrolyte and electrons in the TiO_2 nanolayer. The EAT_Shape_Y dealt with size and branching in the molecular structure, which would enhance the bulk of dyes resulting in sensitized wide-bandgap in nanostructured photoelectrode. The graph density indicated the surface area of the dye, which led to the prolongation of the electron injection into the nanostructured TiO_2 from the dye. X4Av and F05[N-N] were the average valence connectivity and the frequency of two nitrogen atoms at topological distance 5, having positive and negative contributions to the PCE, respectively.

For the other six datasets, the authors completed a full analysis of the relationships among the descriptors, dye structures, and PCEs, as detailed in the original article. Inspired by the comprehensive discussions for the seven chemical classes, the authors designed ten coumarin dyes due to their low PCEs compared to all other studied chemical classes, in which the designed dyes showed a 20.68%-43.51% increase in PCE values (8.93%-10.62%) compared with the maximum reported experimental PCE value of 7.4%. Krishna and co-workers carried out a systematic investigation of the relationships between seven common kinds of organic dyes and device PCEs for DSSCs. More than 1200 dyes were collected and divided into seven datasets for building various PLS models. However, most of the PLS models exhibited relatively low R^2 values of 0.61-0.75, except for the one for diphenylamine dyes. The PLS algorithm is widely used to solve linear problems and might not be suitable for these datasets. More non-linear model algorithms, such as XGBoost and SVM, could be considered to enhance the model predictability. Furthermore, the authors evaluated the designed sensitizers via DFT calculations, while the device performance is also largely subject to other factors, such as the material interfaces. Experimental validations are more encouraged to determine the device performance of the designed organics.

Wen *et al*. not only established an accurate, robust and interpretable ML model for predicting PCEs based on DFT-calculated descriptors, but also performed a virtual screening and the assessment of synthetic accessibility to identify new efficient and synthetically accessible organic dyes for DSSCs[141]. A database incorporating 223 reported organic dyes with experimental PCEs over 4% was built, along with the relaxed electronic structures optimized at the M06-2X/6-31G(d) level. The input features were comprised of 21 easily obtained descriptors extracted from the ground-state structures and statistical properties, such as orbital levels, atom counts, and dipole moments, which were further augmented by the expensively calculated vibrational, cationic, anionic, and excited-state properties. To achieve a compromise between the calculation costs and model accuracy, two models (models A and B) were built for the next 2 stepwise large-scale screenings, exerting only the simple and all features separately. Four algorithms, namely, RF, GBT, SVM, and ANN, were picked to perform the models. For model A, the ρ values in CV5 were 0.57, 0.57, 0.63, and 0.65, and the ρ values in the test set were 0.68, 0.64, 0.68, and 0.76 for the four algorithms, respectively, signifying that the ANN model had the best accuracy. The extended descriptors were then incorporated to train model B, eventuating ρ values in CV5 of 0.75, 0.76, 0.74, and 0.74, and ρ values in the test set of 0.70, 0.76, 0.77, and 0.78, respectively.

To enhance the prediction accuracy, the heterogeneous ensemble voting regressor model was built from the GBT, SVM, and ANN based on the voting weight of 4:7:4. The GBT-SVM-ANN model achieves partially higher accuracies with ρ values in CV5 and a test set of 0.70 and 0.79 for model A and 0.76 and 0.78 for model B, respectively. Then, 20 donor groups (D), 12 π groups (π), 6 acceptor groups (A), and 6 auxiliary acceptor groups (Aa) were permutated to form 10080 molecular structures in the configurations of both typical electron donor-π-bridge-electron acceptor (D-π-A) and D-Aa-π-A with the additional electron-withdrawing unit (Aa). Among them, 9886 were left with the converged optimizations in DFT calculations. The 2-stage screening were then performed by adopting the two GBT-SVM-ANN models to predict the structures, emanating 500 molecules left with their predicted PCEs of over 8%. In addition to the PCEs, the authors also considered the synthetic accessibility (SA score) developed in reference[206] based on molecular complexity and finally shortlisted 8 prominent dyes with SA scores of less than 4.

In an earlier study, Venkatraman *et al*. explored the absorption shift of a dye sensitizer influenced by the adsorption on TiO_2[207]. A total of 1961 absorption data of dyes adsorbed on TiO_2 in various solutions were collected from ~ 500 studies. The natures of their spectral shift were determined by red shift (R), blue shift (B), and unchanged (N) with the threshold of less than 10 nm of the maximum absorption difference, in which the unchanged (N) was further grouped into NR (positive difference below 10 nm) and NB (negative difference over -10 nm). The authors considered three classification schemes. The first was the B, N, and R classification problem with the class distribution (2:1:1). The second problem involved B and NR with a 1:1 distribution, while the third was the NB and R classification with a distribution of 2.5:1. The atom-bond sequences and topological indices were generated in 2060 numbers as the input features using the ISIDA Fragmentor 2017[208] and RDKit[64], leaving 200 features remaining after correlation filtering. The dataset was randomly split into training (75%) and test (25%) sets. Six classification algorithms were implemented, including linear discriminant analysis (LDA), KNN, SVM, CART, RF, and GBT, in which the RF models gained the best accuracies both for the training and test sets: 71% and 76% for the B:N:R classification, 76% and 80% for the NB:R classification and 76% and 80% for the B:NR classification, respectively. In order to test the performance of the ML models, three dyes (quercetin, 2,5-dihydroxytetraphthalic acid and carminic acid) in 5 solvents, including dimethylformamide, acetonitrile, toluene, tetrahydrofuran, and methanol, were examined (14 cases in total), with 81%, 81% and 71% predicted by the RF models in the B:NR, NB:R and B:N:R classifications, respectively.

Our work concerning the data-driven discovery of novel DSSCs features the ML-aided design of new sensitizer materials based on BODIPY[93] and N-annulated perylene (N-P)[92]. Taking the case of BODIPY as an example, we collected a total of 58 BODIPY sensitizers that could be divided into horizontal and vertical types, with both types consisting of 29 samples. In contrast to the work of Krishna[90], we generated descriptors as much as possible to depict the structures of the sensitizers using Dragon and JChem software, resulting in 5515 dimensions of the features. A GA was employed to filter the descriptors for the two types of dataset, which were used to construct two LR models (horizontal and vertical models). The performance of the two models targeting PCEs achieved correlation coefficients ρ of 0.926 and 0.898 in LOOCV and 0.895 and 0.928 in test validations. It is noteworthy that the feature interpretations were very useful in designing new structures with quantum-based validations.

In the horizontal model, for example, the most important descriptor, Mor14p (see details in Section S2 and Figures S3 and S4), indicated that more conjugated structures and a larger number of C-S pairs contributed to the PCE values, stemming in the attachment of the groups, such as benzodithiophene, dithienothiophene, thiophene and similar. An additional C≡C bond and methoxy groups that are near the B atom in the BODIPY core were added under the interpretations of the descriptors nTD and F05[O-B]. According to the mapping fragments of the descriptors, new potential sensitizers were then designed based on the sensitizer structure with the highest PCE in the dataset for each type. The designed structures were further validated using quantum-based evaluations, which revealed that the new candidate possessed the more conjugated structures, larger absorption spectra, faster electron injection efficiencies, and better performance in terms of short-circuit current density (J_{sc}) and open-circuit voltage (V_{oc}). The model prediction and quantum-based validation of the designed candidates shared the same results regarding the promising performance. Despite the complete model analysis and the continuous DFT validations, two main deficiencies still exist, namely, a lack of sufficient samples and experimental validations, which may constrain the further applications of the models.

The exploitation of new dye structures might have reached a bottleneck due to the scant absorption ability of singular organic molecules. The introduction of a co-sensitizer to expand the absorption capability is a practice alternative to enhance the performance of such devices. Cooper *et al*. probed the discovery of new co-sensitizer materials with panchromatic optical absorption for DSSCs using a design-to-device approach integrated with a high-throughput screening and text-mining method[209]. In total, 9431 dye materials were generated via the text-mining software ChemDataExtractor[210], including their chemical structures, maximum absorption wavelengths, and molar extinction coefficients. A stepwise screening based on statistics was then processed to shortlist the potential dye structures. In the initial stage, small molecules, organometallic dyes, and the materials that have no absorption in the solar spectra were first removed, leaving 3053 organic dyes. Two key structure-property data indicated the presence of a carboxylic acid group and a sufficiently large molecular dipole moment (over 5 D), which were applied to filter the remaining dyes, resulting in 309 dyes being shortlisted. This information suggested that the dyes contain a high-performance DSSC anchoring group, leading to the effective adsorption onto TiO_2 surfaces to create working electrodes, while the latter information was required for the effective intramolecular charge transfer after photoexcitation.

Afterwards, the authors developed a dye matching algorithm for further screening. Based on the known optical absorption peak wavelengths and extinction coefficients, each potential dye combination for co-sensitization could be ranked using a quality score. The algorithm ensured that the dye combination avoided the optical absorption overlap, exhibited panchromatic absorption, and had an improvement compared to any single dye, yielding 33 remaining dyes. Lately, the highest occupied molecular orbital (HOMO) and lowest-unoccupied molecular orbital (LUMO) energy levels were inspected by DFT. The dye candidate pool was reduced to 29 dyes after consideration of the criteria of LUMO energy level greater than -3.74 eV (TiO_2 conduction band in a vacuum) and HOMO energy level below -4.85 eV (I^-/I_3 redox potential in a vacuum), which was essential for forming a standard DSSC device integration. At the final screening stage, 5 dyes, comprising *C1*, *8c*, *XS6*, *15*, and *H3*, were retained, considering the ease of synthesis and availability for the next stage of experimental validations. The PCE (η) ratio η_{dye}:η_{N719} was used to indicate the photovoltaic performance of the five potential co-sensitizers compared to a reference sample N719 dye, in which the co-sensitizer combination *XS6* and *15* gained the largest ratio of 0.92. The atomic force microscopy (AFM) and X-ray reflectometry were further employed to characterize the co-sensitizers, indicating that the combination *XS6* and *15* possessed the lowest aggregate coverage of 0.3%, the smallest dye-layer thickness of 19 Å, and the highest surface coverage over 70%, which correlated to the best performance in the filtered co-sensitizers.

Data-driven progress in OSCs

In spite of the long history of OSC studies, ML-related ones were scarce until 2018, which might be traced to the complex systems whose active layers mostly comprise binary or even ternary organic systems. Benefitting from the widespread of AI techniques and the stringent requirement for more efficient OSCs materials, ML and DL techniques are blooming to accelerate the process of discovering new potential PV materials for OSC devices. The main challenges issued from the AI work in the OSC field are mainly focused on 1) the representations of complex organic structures, particularly in blend systems, 2) the poor performance of the ML models with the currently maximum R^2 in the test set lower than 0.77[211], and 3) how to apply models to experiments. To date, the blend active layer system, especially for the binary organic framework of the polymer as an electron donor (D) and the non-fullerene acceptor (NFA) as an electron acceptor (A), has achieved the most promising PCE values of over 18% in OSC devices, better than the single or ternary organic system. Most attention in the OSC community has been focused on this organic system. The typical ML publications of OSCs are summarized in Table 7.

Very recently and impressively, Kranthiraja *et al*. manually collected 566 polymer-NFA organic photovoltaic (OPV) samples from 253 publications before the end of 2018 to predict PCEs[99]. The descriptors were composed of the materials properties (MP) and FPs of the polymers (p) and NFA (n), in which MP included the HOMO, LUMO, bandgap, and molecular weight. The RF model was built up and examined by CV5 with the highest ρ value of 0.85, compared to the values of 0.59, 0.79, 0.85, 0.84, and 0.81 for ANN, GBT, SVM, KRR, and KNN, respectively. Based on the robust RF model, descriptor importance was calculated for the polymer-NFA OPV materials. It was found that the sum of the importance of polymer-relating MP(p) only accounted for 6.9% in the whole descriptors, leading to a constant ρ value of 0.85 for the RF model after removing the MP(p) descriptors of the polymer, which was encouraged by the good ρ value of 0.78 for the bandgap RF model and 0.73 for the HOMO RF model that was built solely from FP(p). Given the acceptable RF model, the

Table 7. Typical ML publications of OSCs

Publication	Sample	Feature	ML Task	ML Algorithm	(Best) Model Performance
Kranthiraja *et al* [99]	566 reported polymer-NFA OPV samples	Materials properties and fingerprints	Predict PCE	ANN, GBT, SVM, KRR, KNN, and RF (best)	CV5 ρ 0.85
Wu *et al*. [148]	565 reported donor-acceptor pairs	Fingerprints	Predict PCE	LR, LRC, RF (best), ANN, and GBT	CV10 MAE 0.832
Zhao *et al* [212]	566 reported organic donor-acceptor pairs	Fingerprints and quantum-based properties	Predict PCE	KNN (best), KRR, and SVM	LOOCV ρ 0.72
Meftahi *et al*. [213]	344 samples from Harvard Photovoltaic Dataset	Signature descriptors	Predict PCE, V_{OC}, J_{SC}, bandgaps	BRANNLP	Training R^2 0.57~0.94 Test R^2 0.49~0.78
Lee *et al*. [211]	124 fullerene derivatives-based ternary OSCs samples	Theoretical orbital energies	Predict PCE	RF (best), GBT, KNN, LR, SVM	LOOCV R^2 0.66 Test R^2 0.77
David *et al*. [218]	1850 reported device data	17 experimental conditions	Predict device stability	SMOreg	LOOCV ρ 0.74~0.82 Test ρ 0.66~0.73
Du *et al*. [221]	100 fabricated device data	10-dimensional processing parameters	Predict photovoltaic performance	GP	Test RMSE 0.012~1.175
Majeed *et al*. [231]	20000 simulated device data	Light JV and dark JV curves	Predict electron and hole mobility, tail slope, and trap density	Deep neural network	
Pokuri *et al*. [232]	65000 simulated morphologies	Images	Classify morphology	CNN	Accuracy 95.80%
Sahu *et al*. [233]	300 reported small-molecule OPVs	28 DFT descriptors	Predict PCE	GBRT (best), ANN, KNN	ρ 0.80
Padula *et al*. [163]	249 reported organic donor-acceptor pairs	DFT descriptors and fingerprints	Predict experimental photo voltaic parameters	KNN	ρ 0.68
Sahu *et al*. [176]	300 reported OPVs	Experimental device parameters and DFT descriptors	Predict PCE, V_{OC}, J_{SC}, FF	GBRT (best), RF	LOOCV ρ 0.64~0.78
Sahu *et al*. [234]	280 reported small-molecule OPVs	13 DFT descriptors	Predict PCE	LR, KNN, ANN, RF, GBT (best)	LOOCV ρ 0.79
Padula *et al*. [235]	320 reported organic donor-acceptor pairs	DFT descriptors	Predict PCE	KRR (best), GPR, SVR, KNN	LOOCV ρ 0.78
Nagasawa *et al*. [236]	1200 reported cell devices	1000 experimental parameters and fingerprints	Predict PCE	ANN, RF (best)	ρ 0.62
Pyzer-Knapp *et al*. [182]	266 reported donor materials	Fingerprints	Predict PCE, V_{OC}, J_{SC}, bandgap	GP	ρ 0.51-0.68
Lopez *et al*. [68]	51000 non-fullerene acceptors	106 common moieties	Predict HOMO, LUMO	GP	ρ 0.81-0.93

ML: Machine learning; OSCs: organic solar cells; NFA: non-fullerene acceptor; OPV: organic photovoltaic; PCE: power convection efficiency; ANN: artificial neural network; GBT: gradient boosting tree; SVM: support vector machine; KRR: kernel ridge regression; KNN: K-nearest neighbor; RF: random Forest; CV5: 5-fold Cross-validation; ρ : pearson correlation coefficient; LR: Linear regression; LRC: logistic regression classification; CV10: 10-fold cross-validation; MAE: mean average error; LOOCV: leaving-one-out Cross-validation; V_{OC}: open circuit voltage; J_{SC}: short circuit current density; BRANNLP: bayesian regularized artificial neural network with Laplacian prior; R^2: determination coefficient; SMOreg: sequential minimal optimization regression GP: gaussian process; GPR: gaussian process regression; RMSE: root mean squared error; JV: current density-voltage (JV) measurements; CNN: convolutional neural network; DFT: density functional theory; GBRT: gradient boosting regression tree; FF: fill factor; HOMO: highest occupied molecular orbital; LUMO: lowest unoccupied molecular orbital.

authors performed a virtual screening process suitable for the representative NFA molecules (abbreviated as ITIC and IT-4F) based on 200932 polymers combined from 382 donor units and 526 acceptor units that were furtherly fragmented from the structures of 566 polymer samples, in which only 1098 (~0.5% in the virtual space) have been reported in current publications.

To corroborate the model predicting result, the second-ranked polymer, labeled as PBDT(SBO)TzH, in the predicted PCE list of polymer-ITIC was selected for the synthesis, which consisted of benzodithiophene as the donor unit and thiazolothiazole (Tz) as that acceptor unit that were solubilized by sulfur-bridged 2-butyloctyl (BO) chains (SBO). However, the experimental PCE values in polymer-ITIC and -IT-4F were only 4.44% and 3.42% compared to the predicted values of 11.1% and 10.5%, which might be traceable from the poor solubility and rapid aggregation that was presumably not considered in the RF model. To ameliorate the flaws of PBDT(SBO)TzH, 4 variants were designed by replacing the SBO group that was responsible for the aggregation behavior and the varying the chains of the alkylthiophene-flanked Tz group that accounted for the poor solubility. One of the designed structures, marked as PBDTTzEH, showed a relatively similar experimental PCE value (10.10%) to the predicted one (11.17%), though the others still exhibited poor experimental PCE values of 2.15%, 3.97%, and 2.34% compared to the predicted values of 10.28%, 10.72%, and 10.70% due to the two unpromoted imperfections.

Experimental characteristics were measured to identify why PBDTTzEH had excellent performance. The $J-V$ curves indicated the highest J_{sc} value of 16.47 mA cm^{-2} among the 5 polymers and the secondarily large fill factor value of 0.65, while the electrodeless Xe-flash time-resolved microwave conductivity test showed the most efficient mobility both for holes and electrons, which certainly correlated with its superior PCE. In particular, according to the images from AFM, PBDTTzEH exhibited a well-interdigitated morphology, which signaled no aggregation. The work of Kranthiraja not only provided a systematic ML analysis for polymer samples but also performed a detailed experimental validation. Such work may establish a good paradigm of how to use ML to accelerate the discovery of new potential polymer materials for the OSC community.

Another similar example could be seen in the work of Wu *et al*.[148] [Figure 8], which explored potential donor and acceptor materials for OSCs. They extracted 565 donor-acceptor pairs from 274 publications as the data samples to predict PCEs, in which each structure in both the donors and acceptors was divided into several fragments that were furtherly encoded by FPs. As a result, there were 31, 14, 27, and 14 in number for the 1-4 fragments for the donors and 30, 18, 6, 22, and 35 for the 1-5 fragments for the acceptors. Therefore, the description of each donor-acceptor sample was expressed by the FP's combinations of fragments. For the ML modeling, various algorithms of LR, LRC, RF, ANN, and GBT were performed based on the training data composed of ~85% of all samples, where the RF and GBT models exhibited more satisfactory performance with ρ values of 0.70 and 0.71 than the values below 0.60 for the other models. A 10-fold cross-validation was appended to evaluate the five models, leading to the lowest MAE value of 0.832 for the RF model and 1.653 for the GBT model compared to the values of 2.1-2.6 for the others, which signaled the robustness of the RF and GBT models.

By targeting the three high (> 11%)/moderate/low (< 7%) groups divided by the PCE values, the authors represented the classification models, in which the RF model still had the highest accuracy of 60.23%, especially the accuracy of 65.2% in the case of the high-label group. Given the favorable performance of the RF and GBT models, virtual screening was conducted to predict the PCE values of the automatically generated 32076000 donor-acceptor pairs that were permuted from the fragments of the donors and acceptors in the collected sample set. Following the criteria of easy synthesis and highly predicted PCE values of over 10%, the authors selected six donor-acceptor binary systems composed of two experimentally reported donors abbreviated as PM6 and PBDB-Y and three undiscovered acceptors denoted as Y-ThCN, Y-ThCH3, and Y-PhCl. With the exception of the PM6:Y-ThCH3 system (6.67% in experiments *vs*. 11.14% and 10.41% predicted by the RF and GBT models, respectively), their experimental PCE values are highly consistent with their predicted values, with the experimental PCE values for PM6:Y-ThCN, PM6:Y-PhCl, PBDB-T:Y-ThCN, PBDB-T:Y-ThCH3 and

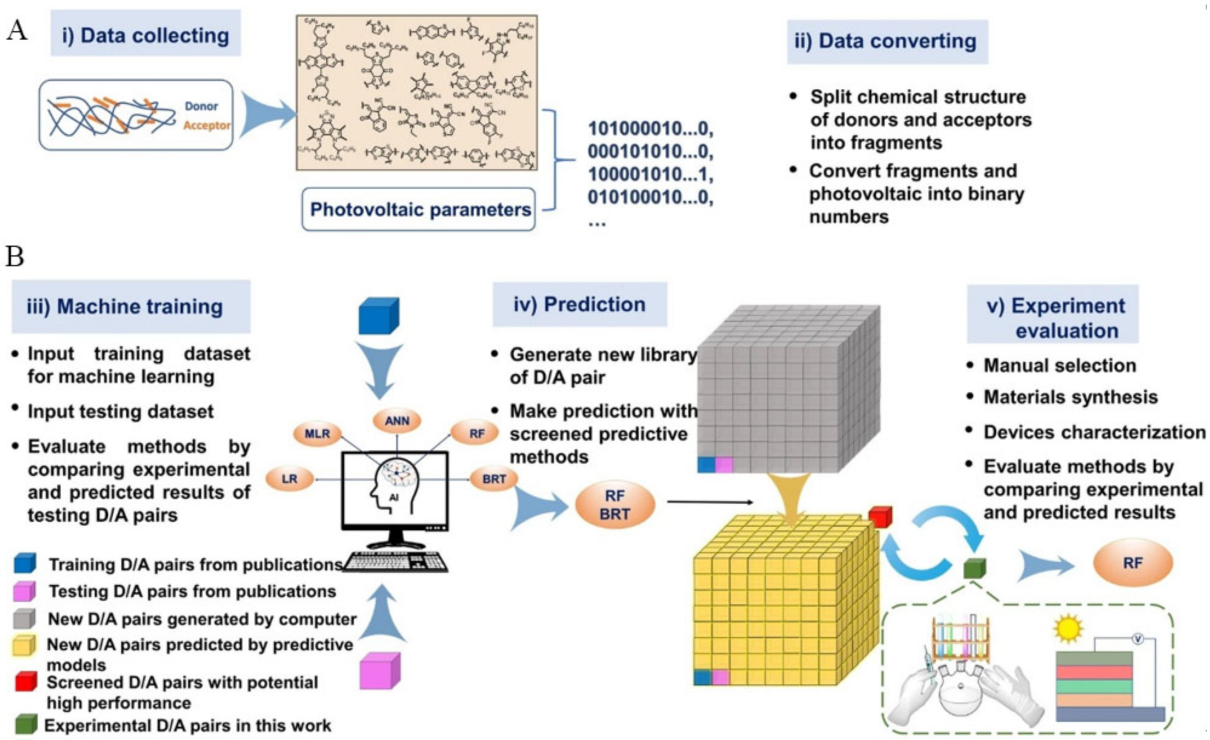
A
i) Data collecting
Donor
Acceptor
Photovoltaic parameters
101000010...0,
000101010...0,
100001010...1,
010100010...0,
...
ii) Data converting
• Split chemical structure of donors and acceptors into fragments
• Convert fragments and photovoltaic into binary numbers
B
iii) Machine training
• Input training dataset for machine learning
• Input testing dataset
• Evaluate methods by comparing experimental and predicted results of testing D/A pairs
ANN
MLR
RF
LR
BRT
AI
iv) Prediction
• Generate new library of D/A pair
• Make prediction with screened predictive methods
RF
BRT
v) Experiment evaluation
• Manual selection
• Materials synthesis
• Devices characterization
• Evaluate methods by comparing experimental and predicted results
RF
Training D/A pairs from publications
Testing D/A pairs from publications
New D/A pairs generated by computer
New D/A pairs predicted by predictive models
Screened D/A pairs with potential high performance
Experimental D/A pairs in this work
V

Figure 8. (A) Schematic of collecting experimental data and converting chemical structures to digitized data. (B) Schematic of machine training, prediction, and method evaluation. Reproduced with permission from Wu *et al.*[148], npj Comput. Mater. **6** (2020). Copyright 2020 Springer Nature.

PBDB-T:Y-PhCl of 13.18%, 15.71%, 11.02%, 11.08% and 11.19% along with the predicted values of 11.56%, 13.30%, 12.73%, 12.49% and 12.55% from the RF models and 10.52%, 13.33%, 11.49%, 11.64% and 11.32% from the GBT models, respectively.

As discussed in the descriptor generation section, most input variables in the collected data are relevant to the processes of synthesis or testing, especially when the samples are sourced from experimental publications, which are far away from the molecular structures. To identify the relationship between material structures and their experimental properties, the descriptors depicting active layer structures are essentially needed, while the descriptor-based studies have been involved in the above cases. In such an instance, it is important to generate useful descriptors representing the structural information as the input variables for model building in the whole ML procedure. In the character of an organic structural scheme, particularly a binary or even ternary arrangement, describing such a complex organic absorber system in a numeric language remains a long-term crucial challenge, but also a promising and effective aspect of promoting the performance of ML models considering the large variety of descriptor choices that have been summarized in the descriptor generation section.

In the work of Zhao *et al.*[212], different kinds of descriptors were investigated for their effects in three ML models with the inclusion of KNN, KRR and SVM, in which the authors categorized them into structural (FPs) and physical (quantum-based) properties, including energy levels, molecule size, absorption, dipole moment, rotatable bonds and the partition coefficient between n-octanol and water, which was labeled as the XLOGP3 descriptor. The dataset included 566 organic donor-acceptor pairs composed of 513 donors and 33 acceptors. It is noteworthy that the authors refined the distance definition of the donor-acceptor pairs for the distance concept in the KNN and the kernel expressions in KRR and SVM, based on the linear distance combination weighted by the physical and structural descriptors of donors, acceptors, and whole systems.

Starting from five physical descriptors, including HOMO-D (where D is donor) to predict the PCE values, LUMO-D, LUMO-A (A is acceptor), reorganization energies of the polymer and acceptor, the LOOCV ρ values of KNN, KRR, and SVM were all below 0.5, while the maximum value could reach as high as 0.72 in the case of KNN after adding two structural descriptors. Although more physical descriptors were considered sequentially, appending new variables, even the terms under more computational cost, did not trigger an improvement in the models. This indicates that the ML models solely based on physical properties might not be useful for practical purposes, since most encoded information in the physical properties was already involved in the structural FPs. However, to balance the model interpretation and predictivity that were represented by the physical properties and FPs, respectively, retaining the amount of interpretable and simply calculated physical properties was still necessary in the ML models. Under this consideration, the optimal descriptor selection, though not suitable for all cases of OSCs, might be a mixture of physical properties and FPs.

Laying aside the traditionally and commonly used organic representations, Meftahi *et al.*[213] employed the so-called signature descriptors proposed by Pablo *et al.*[214] in 2013 into the ML work of predicting the quantum-based properties (such as energy levels) and the Scharber-model-based results[215] (such as PCE, J_{sc} and V_{oc}) for 344 small molecule and polymer electron donors and acceptors, in which the dataset, named as Harvard Photovoltaic Dataset (HOPV15), was collected by Lopez *et al.* under their massive DFT calculations[69]. Complimented by the Cahn-Ingold-Prelog priority rules and directed acyclic graph-based definitions, the signature descriptors could be generated as thousands of substructures for each organic sample regardless of the structural complexity in a matter of minutes. The so-called Bayesian regularized artificial neural network with the Laplacian prior (BRANNLP) algorithm was used to perform the model building, as well as feature selection based on the embedded ability within L1 regression, which was implemented in the CSIRO-Biomodeller package and TensorFlow[216,217]. The neural network was composed of only one hidden layer coupled with the input layer containing descriptors and the output layer for predicting the target, contrary to the large and complex framework in DL. All the Scharber model-based results were predicted via signature descriptors, leaving the R^2 values of 0.72 (PCE), 0.65 (V_{oc}), 0.57 (J_{sc}), 0.87 (HOMO), 0.94 (LUMO) and 0.83 (bandgap) in the training set and the same sequential values of 0.78, 0.58, 0.60, 0.49, 0.67 and 0.65 in the test set. With the exception of the case of J_{sc}, all the models exhibited robust performance and admirable predictive ability, which successfully leveraged resource-intensive DFT calculations into the larger regions of materials space at much lower computing costs. Due to the structural complexity, more informative descriptors for organics are urgently required for ML studies, in which Meftahi's work has provided a good guide for us.

Despite the broad research in the OSC field, there is a significant lack of ML-related studies for the ternary system due to its complexity, in which only one publication[211], to the best of our knowledge, could be searched on the Web of Science. In Lee's work[211], a dataset of 124 fullerene derivatives-based ternary OSCs samples, regardless of the blend formations such as the composition of either one donor/two acceptors (D:A1:A2) or two donors/one acceptor (D1:D2:A) in the active layer, were constructed from the current literature, along with the theoretical orbital energies of donors, acceptors, and the whole systems. Targeting the PCE, the regression models of RF, GBT, KNN, LR, SVM, and the 99 training samples were undertaken, eventuating in the best performance with LOOCV R^2 of 0.66 and test R^2 of 0.77 for the RF model. The other models exhibited the poor LOOCV R^2 values lower than 0.60 and test R^2 values from 0.25 to 0.73. Additionally, the classifier models of RF, extra tree classifier (ETC), KNN, SVM, ANN and DT algorithms were also performed, rendering the highest LOOCV and test accuracies of 79% and 76%, respectively, for the RF model. Given the outstanding performance, the feature importance of the RF model was extracted, showing the largest contribution of LUMO-D1 (denoted as LUMO of D1) and the second of HOMO-D1. The logical flowchart of one subtree in the RF model was visualized, signifying the key attributes of LUMO-D1, HOMO-D1, and HOMO-A1, which was also coherent with the results shown in other experimental studies according to the authors. Despite lacking further extensions and applications, Lee *et al.* presented guidance and initiation for the ML researchers that may have an interest in ternary OSC systems[211].

The analysis of the whole OSC device structure based on a large-scale dataset constituting both single and blend active layers had not been reported before the work of David *et al.*[218]. A dataset comprising 1850 device data was prepared, in which most were obtained from the Danish Technical University ranging from 2011 to 2017 and the remaining were manually scraped between 2017 and 2019. Regarding device stability, the numeric data of T_{80} that was defined as the time taken for the device to reach 80% of the initial efficiency (E_0) were extracted along with T_{S80} that was the time taken for the device to reach 80% of the stabilized value. Fully 17 categorical features were acquired, covering the device structures and materials, encapsulation, substrate type, test protocols, environmental conditions, light sources, and the measurement conditions, such as temperature, light level, bias condition, and relative humidity.

Considering the 2 different testing conditions based on the International Summit on Organic Photovoltaic Stability (ISOS) protocols[219], the dataset involving 1149 samples after carefully data cleansing were treated in three modes: the full dataset with 1149 samples, the data (155) conducted with light soaking (ISOS-L) that relates to photostability, and the data (489) conducted with dark storage studies (ISOS-D) that provides information on the tolerance of the solar cells to oxygen, moisture, other aggressive atmospheric components naturally in air. The sequential minimal optimization regression (SMOreg) algorithm[220] was introduced into ML model building since it had the ability to produce the weights, namely the importance, of each feature, and thence help us to understand the feature significance, in which a positive SMOreg weighting corresponds to a positive influence on stability and the vice versa. The SMOreg model based on whole data signaled the LOOCV ρ of 0.739 and the test ρ of 0.713. The models using ISOS-L and ISOS-D data exhibited the relatively higher LOOCV ρ of 0.819 and 0.767 and the test ρ of 0.734 and 0.659.

Given the quantified significance from the weighting in SMOreg, several important features were identified. For instance, the features that most positively influenced the stability, namely, T_{80}, in the whole dataset were the choices of the materials in the first transport layer and active layer. Furthermore, the use of LED lights would benefit T_{80}, while all the ISOS testing conditions and the light intensity would damage the stability. For the case of ISOS-L, the most influential features were the device components (such as substrate, transport layers and active layers electrodes), layer materials, and light source, while layer materials, device architecture, and encapsulation method were the most affecting attributes in ISOS-D dataset. In addition to the research focus on the stability, the same methodology was also applied to predicting the initial efficiency E_0 using SMOreg and full data (1347 samples), deriving the LOOCV ρ of 0.739 and the MAE of 0.605%, along with the most significant features involving the choice of active layer and tandem configuration.

Identical to the robotic work of Zhao *et al.* in the PSC field[84], Du *et al.* also utilized a high-throughput robot-based platform, "AMANDA Line One", to realize the superior precise control in experimental conditions at a very large scale so as to form high-quality and continuous sample points, which could also be expanded to the optimization in experimental details for any solution organic semiconductor and interface materials[221]. For this purpose, the authors fabricated around 100 OSC devices within photovoltaic performance (such as PCE, V_{oc}, J_{sc} and FF) and performed 50-h photostability testing varying in ten-dimensional processing parameters covering D (donor PM6):A (acceptor Y6) ratio, concentration, spin speed, active layer, annealing temperature, active layer annealing time, solvent additives, solvent additives volume, electronic transport layer (ETL) materials, ETL annealing temperature and time, which totally consumed only ~70 h. From the point of statistical analysis of the observed data, several optimum processing parameters were exploited, *e.g.*, a D:A weight ratio of 1:1.2, a low thermal annealing temperature and the others for higher efficiency, as well as high spin speed and active layer annealing temperature below 100 °C for longer stability. Furthermore, GP was employed to build the ML models to predict the four photovoltaic parameters, obtaining RMSEs in the test set of 1.175 (PCE), 0.012 (V_{oc}), 0.055 (FF), and 0.903 (J_{sc}).

CONCLUSION AND OUTLOOK

In this review, we have described the integral ML and DL training progress in section 2 and overviewed the recent ML and DL applications in the three fields of PSCs, DSSCs, and OSCs in section 3. Before training an ML/DL model, the first step is to collect samples along with their properties to form the dataset. The data sources in the most current publications are largely dependent on mature experimental and calculation databases, like the Materials Projects, ICSD, OQMD, and MPDS. With an increasing spread of high-throughput computations[83] and robotic experiments[84], more and more datasets with consistency and high quality will be produced and mined at the lab scale. To enhance the model performance, key attention should be devoted not only to the structural descriptors, such as the SMILE, molecular descriptors, fingerprints, and atomic descriptors, but also to the state-of-art modeling technologies, e.g., GCNN framework[120] and SISSO method[124]. Regarding model algorithms, the widely applied methods are sliced into the ensemble algorithms, especially GBM derivatives and the DL models, such as deep ANN and CNN. As the algorithms develop, we may see more occurrences of more predictive and advanced model algorithms in the future, such as GAN, VAE, RNN, and LSTM networks. Given an established model, the most practiced method to apply the model is to perform high-throughput screening to filter the potential candidates, in which the search space should be restrained and the candidates need to be shortlisted by domain knowledge. Another method is to understand the established models by combining domain knowledge and feature interpretation via various analysis tools, such as the SHAP method[39,143].

In summary, with the fast-developing ML and DL technologies, data-driven methods combined with domain knowledge will exhibit more robust performance and accurate prediction power in materials science beyond photovoltaic fields, with the potential to be an indispensable analysis tool for both experiments and quantum-based computations in the future.

DECLARATIONS

Availability of data and materials

Supporting information available: details of outlier detection algorithms; Illustration for descriptors Mor14p, Mor24m, R2s; Atomic parameters.

Authors' contributions

Wrote the manuscript: Lu T
Supervised this manuscript: Li M, Lu W, Zhang TY

Conflicts of interest

The authors declared that there are no competing financial interest.

Financial support and sponsorship

This study was supported by the National Key Research and Development Program of China (No.2018YFB0704400), the Key Research Project of Zhejiang Laboratory (No.2021PE0AC02), and Shanghai Pujiang Program (21PJD024).

Ethical approval and consent to participate

Not applicable.

Consent for publication

Not applicable.

Copyright

REFERENCES

1. Hadadian M, Smått J, Correa-baena J. The role of carbon-based materials in enhancing the stability of perovskite solar cells. *Energy Environ Sci* 2020;13:1377-407. DOI
2. Liu Y, Li Y, Wu Y, et al. High-efficiency silicon heterojunction solar cells: materials, devices and applications. *Mater Sci Eng: R: Rep* 2020;142:100579. DOI
3. Kim M, Ham S, Cheng D, Wynn TA, Jung HS, Meng YS. Advanced characterization techniques for overcoming challenges of perovskite solar cell materials. *Adv Energy Mater* 2021;11:2001753. DOI
4. Li H, Li F, Shen Z, et al. Photoferroelectric perovskite solar cells: principles, advances and insights. *Nano Today* 2021;37:101062. DOI
5. L. R. Devereux, J. M. Cole. in Data science applied to sustainability analysis, edited by Jennifer Dunn and Prasanna Balaprakash (Elsevier, 2021), pp. 129. DOI
6. Kojima A, Teshima K, Shirai Y, Miyasaka T. Organometal halide perovskites as visible-light sensitizers for photovoltaic cells. *J Am Chem Soc* 2009;131:6050-1. DOI PubMed
7. Zhang F, Lu H, Tong J, Berry JJ, Beard MC, Zhu K. Advances in two-dimensional organic-inorganic hybrid perovskites. *Energy Environ Sci* 2020;13:1154-86. DOI PubMed PMC
8. Kim G, Min H, Lee KS, Lee DY, Yoon SM, Seok SI. Impact of strain relaxation on performance of α-formamidinium lead iodide perovskite solar cells. *Science* 2020;370:108-12. DOI PubMed
9. Green MA, Dunlop ED, Hohl-ebinger J, Yoshita M, Kopidakis N, Hao X. Solar cell efficiency tables (Version 58). *Prog Photovolt Res Appl* 2021;29:657-67. DOI
10. NREL, Best research-cell efficiency chart. Available from: https://www.nrel.gov/pv/cell-efficiency.html [Last accessed on 8 Jun 2022]
11. Luo Q, Wu R, Ma L, et al. Recent advances in carbon nanotube utilizations in perovskite solar cells. *Adv Funct Mater* 2021;31:2004765. DOI
12. Luo D, Su R, Zhang W, Gong Q, Zhu R. Minimizing non-radiative recombination losses in perovskite solar cells. *Nat Rev Mater* 2020;5:44-60. DOI
13. Wu T, Liu X, Luo X, et al. Lead-free tin perovskite solar cells. *Joule* 2021;5:863-86. DOI
14. O'regan B, Grätzel M. A low-cost, high-efficiency solar cell based on dye-sensitized colloidal TiO2 films. *Nature* 1991;353:737-40. DOI
15. Zeng K, Tong Z, Ma L, Zhu W, Wu W, Xie Y. Molecular engineering strategies for fabricating efficient porphyrin-based dye-sensitized solar cells. *Energy Environ Sci* 2020;13:1617-57. DOI
16. Kakiage K, Aoyama Y, Yano T, Oya K, Fujisawa J, Hanaya M. Highly-efficient dye-sensitized solar cells with collaborative sensitization by silyl-anchor and carboxy-anchor dyes. *Chem Commun (Camb)* 2015;51:15894-7. DOI PubMed
17. Tang CW. Two-layer organic photovoltaic cell. *Appl Phys Lett* 1986;48:183-5. DOI
18. Armin A, Li W, Sandberg OJ, et al. A history and perspective of non-fullerene electron acceptors for organic solar cells. *Adv Energy Mater* 2021;11:2003570. DOI
19. Luo Z, Liu T, Yan H, Zou Y, Yang C. Isomerization strategy of nonfullerene small-molecule acceptors for organic solar cells. *Adv Funct Mater* 2020;30:2004477. DOI
20. Zheng Z, Yao H, Ye L, Xu Y, Zhang S, Hou J. PBDB-T and its derivatives: a family of polymer donors enables over 17% efficiency in organic photovoltaics. *Mater Today* 2020;35:115-30. DOI
21. Mishra A. Material perceptions and advances in molecular heteroacenes for organic solar cells. *Energy Environ Sci* 2020;13:4738-93. DOI
22. Kini GP, Jeon SJ, Moon DK. Latest progress on photoabsorbent materials for multifunctional semitransparent organic solar cells. *Adv Funct Mater* 2021;31:2007931. DOI
23. Zhao C, Wang J, Zhao X, Du Z, Yang R, Tang J. Recent advances, challenges and prospects in ternary organic solar cells. *Nanoscale* 2021;13:2181-208. DOI PubMed
24. Schmidt J, Marques MRG, Botti S, Marques MAL. Recent advances and applications of machine learning in solid-state materials science. *npj Comput Mater* 2019;5. DOI
25. Rajan K. Materials informatics. *Mater Today* 2005;8:38-45. DOI
26. Kohn W, Sham LJ. Self-consistent equations including exchange and correlation effects. *Phys Rev* 1965;140:A1133-8. DOI
27. Hohenberg P, Kohn W. Inhomogeneous electron gas. *Phys Rev* 1964;136:B864-71. DOI
28. Luo S, Zeng Z, Wang H, et al. Recent progress in conjugated microporous polymers for clean energy: synthesis, modification, computer simulations, and applications. *Progress in Polymer Science* 2021;115:101374. DOI
29. Chen C, Zuo Y, Ye W, Li X, Deng Z, Ong SP. A critical review of machine learning of energy materials. *Adv Energy Mater* 2020;10:1903242. DOI
30. Haghighatlari M, Vishwakarma G, Altarawy D, et al. ChemML: a machine learning and informatics program package for the analysis, mining, and modeling of chemical and materials data. *WIREs Comput Mol Sci* 2020;10. DOI
31. Moosavi SM, Jablonka KM, Smit B. The role of machine learning in the understanding and design of materials. *J Am Chem Soc* 2020:20273-87. DOI PubMed PMC
32. Chen L, Pilania G, Batra R, et al. Polymer informatics: current status and critical next steps. *Mater Sci Eng: R: Rep* 2021;144:100595. DOI
33. Masood H, Toe CY, Teoh WY, Sethu V, Amal R. Machine learning for accelerated discovery of solar photocatalysts. *ACS Catal* 2019;9:11774-87. DOI
34. Jia Y, Hou X, Wang Z, Hu X. Machine learning boosts the design and discovery of nanomaterials. *ACS Sustainable Chem Eng*

2021;9:6130-47. DOI

35. Brown KA, Brittman S, Maccaferri N, Jariwala D, Celano U. Machine learning in nanoscience: big data at small scales. *Nano Lett* 2020;20:2-10. DOI PubMed
36. Domingos P. A few useful things to know about machine learning. *Commun ACM* 2012;55:78-87. DOI
37. Halevy A, Norvig P, Pereira F. The unreasonable effectiveness of data. *IEEE Intell Syst* 2009;24:8-12. DOI
38. Jablonka KM, Ongari D, Moosavi SM, Smit B. Big-data science in porous materials: materials genomics and machine learning. *Chem Rev* 2020;120:8066-129. DOI PubMed PMC
39. Xiong J, Shi S, Zhang T. Machine learning of phases and mechanical properties in complex concentrated alloys. *J Mater Sci Technol* 2021;87:133-42. DOI
40. BONEAU CA. The effects of violations of assumptions underlying the test. *Psychol Bull* 1960;57:49-64. DOI PubMed
41. Edgell SE, Noon SM. Effect of violation of normality on the t test of the correlation coefficient. *Psychological Bulletin* 1984;95:576-83. DOI
42. R. G. Lomax, An introduction to statistical concepts. (Mahwah, N.J.: Lawrence Erlbaum Associates Publishers, 2007), p.10. DOI
43. Breunig MM, Kriegel H, Ng RT, Sander J. LOF: identifying density-based local outliers. *SIGMOD Rec* 2000;29:93-104. DOI
44. Liu FT, Ting KM, Zhou Z. Isolation-based anomaly detection. *ACM Trans Knowl Discov Data* 2012;6:1-39. DOI
45. Rousseeuw PJ. Least median of squares regression. *J Am Stat Assoc* 1984;79:871-80. DOI
46. Rousseeuw PJ, Driessen KV. A fast algorithm for the minimum covariance determinant estimator. *Technometrics* 1999;41:212-23. DOI
47. Schölkopf B, Platt JC, Shawe-Taylor J, Smola AJ, Williamson RC. Estimating the support of a high-dimensional distribution. *Neural Comput* 2001;13:1443-71. DOI PubMed
48. Chang C, Lin C. LIBSVM: A library for support vector machines. *ACM Trans Intell Syst Technol* 2011;2:1-27. DOI
49. Zhao Y, Hryniewicki MK. Improving supervised outlier detection with unsupervised representation learning. Available from: https://arxiv.org/abs/1912.00290 [Last accessed on 10 Jun 2022]
50. Chen T, Guestrin C. XGBoost: a scalable tree boosting system (2016), https://xgboost.readthedocs.io/en/latest/install.html DOI
51. Dorogush AV, Ershove V, Guilin A. CatBoost: gradient boosting with categorical features support (2018). Available from: https://catboost.ai/docs [Last accessed on 8 Jun 2022]
52. Jain A, Ong SP, Hautier G, et al. Commentary: the materials project: a materials genome approach to accelerating materials innovation. *APL Materials* 2013;1:011002. DOI
53. Zagorac D, Müller H, Ruehl S, Zagorac J, Rehme S. Recent developments in the inorganic crystal structure database: theoretical crystal structure data and related features. *J Appl Crystallogr* 2019;52:918-25. DOI PubMed PMC
54. Saal JE, Kirklin S, Aykol M, Meredig B, Wolverton C. Materials design and discovery with high-throughput density functional theory: The open quantum materials database (OQMD). *JOM* 2013;65:1501-9. DOI
55. Kirklin S, Saal JE, Meredig B, et al. The open quantum materials database (OQMD): assessing the accuracy of DFT formation energies. *npj Comput Mater* 2015;1. DOI
56. P. Villars. Materials platform for data science (2019). Available from: https://mpds.io/ [Last accessed on 8 Jun 2022]
57. Su Y. Materials genome engineering databases (University of Science and Technology Beijing, 2018). Available from: https://www.mgedata.cn/ [Last accessed on 8 Jun 2022]
58. Qian Q, Wang Y, Zhao S. Materials data specification: methods and use cases. *Comput Mater Sci* 2019;169:109086. DOI
59. Tao Q, Xu P, Li M, Lu W. Machine learning for perovskite materials design and discovery. *npj Comput Mater* 2021;7. DOI
60. Ramakrishna S, Zhang T, Lu W, et al. Materials informatics. J *Intell Manuf* 2019;30:2307-26. DOI
61. Groom CR, Bruno IJ, Lightfoot MP, Ward SC. The cambridge structural database. *Acta Cryst* 2016;72:171-9 DOI
62. Grazulis S, Chateigner D, Downs RT, Yokochi AFT, Quiros M, Lutterotti L, Manakova E, Butkus J, Moeck P, Bail AL. Crystallography open database - an open-access collection of crystal structures. *J Appl Crystallogr* 2009;42:726-9 DOI
63. Gómez-Bombarelli R, Wei JN, Duvenaud D, et al. Automatic chemical design using a data-driven continuous representation of molecules. *ACS Cent Sci* 2018;4:268-76. DOI PubMed PMC
64. G. Landrum. RDKit: Open-source cheminformatics (2012). Available from: http://www.rdkit.org/ [Last accessed on 8 Jun 2022]
65. Ramakrishnan R, Dral PO, Rupp M, von Lilienfeld OA. Quantum chemistry structures and properties of 134 kilo molecules. *Sci Data* 2014;1:140022. DOI PubMed PMC
66. Irwin JJ, Sterling T, Mysinger MM, Bolstad ES, Coleman RG. ZINC: a free tool to discover chemistry for biology. *J Chem Inf Model* 2012;52:1757-68. DOI PubMed PMC
67. IBM. World Community Grid. Available from: http://www.worldcommunitygrid.org/ [Last accessed on 8 Jun 2022]
68. Lopez SA, Sanchez-lengeling B, de Goes Soares J, Aspuru-guzik A. Design principles and top non-fullerene acceptor candidates for organic photovoltaics. *Joule* 2017;1:857-70. DOI
69. Lopez SA, Pyzer-Knapp EO, Simm GN, et al. The Harvard organic photovoltaic dataset. *Sci Data* 2016;3:160086. DOI PubMed PMC
70. Venkatraman V, Raju R, Oikonomopoulos SP, Alsberg BK. The dye-sensitized solar cell database. *J Cheminform* 2018;10:18. DOI PubMed PMC
71. Odabaşı Ç, Yıldırım R. Performance analysis of perovskite solar cells in 2013-2018 using machine-learning tools. *Nano Energy* 2019;56:770-91. DOI
72. Odabaşı Ç, Yıldırım R. Machine learning analysis on stability of perovskite solar cells. *Sol Energy Mater Sol Cells* 2020;205:110284. DOI
73. Odabaşı Ç, Yıldırım R. Assessment of reproducibility, hysteresis, and stability relations in perovskite solar cells using machine learning.

Energy Technol 2020;8:1901449. DOI

74. Yılmaz B, Yıldırım R. Critical review of machine learning applications in perovskite solar research. *Nano Energy* 2021;80:105546. DOI
75. D. Systèmes, BIOVIA MATERIALS STUDIO (Dassault Systèmes, 2002-2021). Available from: https://www.3ds.com/products-services/biovia/products/molecular-modeling-simulation/biovia-materials-studio/ [Last access on 8 Jun 2022]
76. Kresse G, Furthmüller J. Efficiency of ab-initio total energy calculations for metals and semiconductors using a plane-wave basis set. *Comput Mater Sci* 1996;6:15-50. DOI
77. Kresse G, Furthmüller J. Efficient iterative schemes for ab initio total-energy calculations using a plane-wave basis set. *Phys Rev B Condens Matter* 1996;54:11169-86. DOI PubMed
78. Kresse G, Hafner J. Ab initio molecular dynamics for liquid metals. *Phys Rev B Condens Matter* 1993;47:558-61. DOI PubMed
79. Kresse G, Joubert D. From ultrasoft pseudopotentials to the projector augmented-wave method. *Phys Rev B* 1999;59:1758-75. DOI
80. Frisch MJ, Trucks GW, Schlegel HB et al. Gaussian 16 Rev. C.01. Available from: https://gaussian.com/citation_b01/ [Last accessed on 10Jun 2022]
81. Hartono NTP, Thapa J, Tiihonen A, et al. How machine learning can help select capping layers to suppress perovskite degradation. *Nat Commun* 2020;11:4172. DOI PubMed PMC
82. Lundberg SM, Erion G, Chen H, et al. From local explanations to global understanding with explainable AI for trees. *Nat Mach Intell* 2020;2:56-67. DOI PubMed PMC
83. Saidi WA, Shadid W, Castelli IE. Machine-learning structural and electronic properties of metal halide perovskites using a hierarchical convolutional neural network. *npj Comput Mater* 2020;6. DOI
84. Zhao Y, Zhang J, Xu Z, et al. Discovery of temperature-induced stability reversal in perovskites using high-throughput robotic learning. *Nat Commun* 2021;12:2191. DOI PubMed PMC
85. Mahmood A, Wang J. Machine learning for high performance organic solar cells: current scenario and future prospects. *Energy Environ Sci* 2021;14:90-105. DOI
86. Kode-Chemoinformatics. Dragon 7 (2021). Available from: https://gaussian.com/citation_b01/ [Last accessed on 8 Jun 2022]
87. Available from: https://match.pmf.kg.ac.rs/electronic_versions/Match56/n2/match56n2_237-248.pdf [Last accessed on 10 Jun 2022]
88. Krenn M, Häse F, Nigam A, Friederich P, Aspuru-guzik A. Self-referencing embedded strings (SELFIES): a 100% robust molecular string representation. *Mach Learn : Sci Technol* 2020;1:045024. DOI
89. Kar S, Roy JK, Leszczynski J. In silico designing of power conversion efficient organic lead dyes for solar cells using todays innovative approaches to assure renewable energy for future. *npj Comput Mater* 2017;3. DOI
90. Krishna JG, Ojha PK, Kar S, Roy K, Leszczynski J. Chemometric modeling of power conversion efficiency of organic dyes in dye sensitized solar cells for the future renewable energy. *Nano Energy* 2020;70:104537. DOI
91. Yap CW. PaDEL-descriptor: an open source software to calculate molecular descriptors and fingerprints. *J Comput Chem* 2011;32:1466-74. DOI PubMed
92. Ju L, Li M, Tian L, Xu P, Lu W. Accelerated discovery of high-efficient N-annulated perylene organic sensitizers for solar cells via machine learning and quantum chemistry. *Mater Today Commun* 2020;25:101604. DOI
93. Lu T, Li M, Yao Z, Lu W. Accelerated discovery of boron-dipyrromethene sensitizer for solar cells by integrating data mining and first principle. *J Mater* 2021;7:790-801. DOI
94. Shemetulskis NE, Weininger D, Blankley CJ, Yang JJ, Humblet C. Stigmata: an algorithm to determine structural commonalities in diverse datasets. *J Chem Inf Comput Sci* 1996;36:862-71. DOI PubMed
95. Cereto-Massagué A, Ojeda MJ, Valls C, Mulero M, Garcia-Vallvé S, Pujadas G. Molecular fingerprint similarity search in virtual screening. *Methods* 2015;71:58-63. DOI PubMed
96. Muegge I, Mukherjee P. An overview of molecular fingerprint similarity search in virtual screening. *Expert Opin Drug Discov* 2016;11:137-48. DOI PubMed
97. Pattanaik L, Coley CW. Molecular representation: going long on fingerprints. *Chem* 2020;6:1204-7. DOI
98. Sun W, Zheng Y, Yang K, et al. Machine learning-assisted molecular design and efficiency prediction for high-performance organic photovoltaic materials. *Sci Adv* 2019;5:eaay4275. DOI PubMed PMC
99. Kranthiraja K, Saeki A. Experiment-oriented machine learning of polymer:non-fullerene organic solar cells. *Adv Funct Mater* 2021;31:2011168. DOI
100. Lo. Mentel. mendeleev – a python resource for properties of chemical elements, ions and isotopes (2014). Available from: https://github.com/lmmentel/mendeleev [Last accessed on 8 Jun 2022]
101. Li C, Hao H, Xu B, et al. A progressive learning method for predicting the band gap of ABO_3 perovskites using an instrumental variable. *J Mater Chem C* 2020;8:3127-36. DOI
102. Ong SP, Richards WD, Jain A, et al. Python materials genomics (pymatgen): a robust, open-source python library for materials analysis. *Comput Mater Sci* 2013;68:314-9. DOI
103. Pilania G, Balachandran PV, Kim C, Lookman T. Finding new perovskite halides via machine learning. *Front Mater* 2016;3. DOI
104. N. Chen, Bond parameter function and application (In Chinese), 1st ed. (CHINA SCIENCE PUBLISHING & MEDIA LTD, Beijing, China, 1976. DOI
105. Slater JC. A simplification of the hartree-fock method. *Phys Rev* 1951;81:385-90. DOI
106. Available from: https://jsc.niic.nsc.ru/ [Last accessed on 10 Jun 2022]
107. Pauling L. The nature of the chemical bond. application of results obtained from the quantum mechanics and from a theory of paramagnetic susceptibility to the structure of molecules. *J Am Chem Soc* 1931;53:1367-400. DOI

108. Quill LL. The chemistry and metallurgy of miscellaneous materials. *J Chem Educ* 1950;27:583. DOI
109. Zachariasen WH. A set of empirical crystal radii for ions with inert gas configuration. *Zeitschrift für Kristallographie - Crystalline Materials* 1931;80:137-53. DOI
110. Sanderson RT. Principles of electronegativity Part I. general nature. *J Chem Educ* 1988;65:112. DOI
111. Beskow G. V. M. Goldschmidt: geochemische verteilungsgesetze der elemente. *Geologiska Föreningen i Stockholm Förhandlingar* 2010;46:738-43. DOI
112. Lu W, Lv W, Zhang Q, Lu K, Ji X. Material data mining in Nianyi Chen's scientific family: material data mining in Nianyi Chen's scientific family. *J Chemom* 2018;32:e3022. DOI
113. Murray JS, Lane P, Brinck T, Paulsen K, Grice ME, Politzer P. Relationships of critical constants and boiling points to computed molecular surface properties. *J Phys Chem* 1993;97:9369-73. DOI
114. Byrd EF, Rice BM. Improved prediction of heats of formation of energetic materials using quantum mechanical calculations. *J Phys Chem A* 2006;110:1005-13. DOI PubMed
115. Rice BM, Byrd EF. Evaluation of electrostatic descriptors for predicting crystalline density. *J Comput Chem* 2013;34:2146-51. DOI PubMed
116. T. Lu. fast machine learning (2021). Available from: https://pypi.org/project/fast-machine-learning/ [Last accessed on 8 Jun 2022]
117. Sun W, Li M, Li Y, et al. The use of deep learning to fast evaluate organic photovoltaic materials. *Adv Theory Simul* 2019;2:1800116. DOI
118. Jang J, Gu GH, Noh J, Kim J, Jung Y. Structure-based synthesizability prediction of crystals using partially supervised learning. *J Am Chem Soc* 2020;142:18836-43. DOI PubMed
119. Chen C, Ye W, Zuo Y, Zheng C, Ong SP. Graph networks as a universal machine learning framework for molecules and crystals. *Chem Mater* 2019;31:3564-72. DOI
120. Xie T, Grossman JC. Crystal graph convolutional neural networks for an accurate and interpretable prediction of material properties. *Phys Rev Lett* 2018;120:145301. DOI PubMed
121. T. Stephens. gplearn: Genetic Programming in Python (2016). Available from: https://gplearn.readthedocs.io/ [Last accessed on 8 Jun 2022]
122. Fortin FA, Rainville FMD, Gardner MA, Parizeau M, Gagné C. DEAP: Evolutionary Algorithms Made Easy *J Mach Learn Res* 13, 2171 (2012). Available from: https://www.jmlr.org/papers/v13/fortin12a.html [last accessed on 10 Jun 2022]
123. Ouyang R, Curtarolo S, Ahmetcik E, Scheffler M, Ghiringhelli LM. SISSO: a compressed-sensing method for identifying the best low-dimensional descriptor in an immensity of offered candidates. *Phys Rev Materials* 2018;2. DOI
124. Bartel CJ, Sutton C, Goldsmith BR, et al. New tolerance factor to predict the stability of perovskite oxides and halides. *Sci Adv* 2019;5:eaav0693. DOI PubMed PMC
125. Varoquaux G, Gramfort A, Pedregosa F, Michel V, Thirion B. Multi-subject dictionary learning to segment an atlas of brain spontaneous activity. *J Mach Learn Res* 2011;12: 2825 DOI
126. Golbraikh A, Shen M, Xiao Z, Xiao Y, Lee K, Tropsha A. Rational selection of training and test sets for the development of validated QSAR models. *J Comput Aided Mol Des* 2003;17:241-53. DOI PubMed
127. Golbraikh A, Tropsha A. Predictive QSAR modeling based on diversity sampling of experimental datasets for the training and test set selection. *Mol Divers* 2000;5:231-43.
128. Chandrashekar G, Sahin F. A survey on feature selection methods. *Comput Electr Eng* 2014;40:16-28. DOI
129. Guyon I, Nikravesh M, Gunn S, Zadeh LA. Feature Extraction. *Fuzziness Soft Comput* 2006;207:778 DOI
130. Ding C, Peng H. Minimum redundancy feature selection from microarray gene expression data. *J Bioinform Comput Biol* 2005;3:185-205. DOI PubMed
131. Peng H, Long F, Ding C. Feature selection based on mutual information: criteria of max-dependency, max-relevance, and min-redundancy. *IEEE Trans Pattern Anal Mach Intell* 2005;27:1226-38. DOI PubMed
132. Ramírez-gallego S, Lastra I, Martínez-rego D, et al. Fast-mRMR: fast minimum redundancy maximum relevance algorithm for high-dimensional big data: fast-mRMR algorithm for big data. *Int J Intell Syst* 2017;32:134-52. DOI
133. Guyon I, Weston J, Barnhill S, Vapnik V. Gene selection for cancer classification using support vector machines. *Machine Learning* 2022;46:389-422. DOI
134. Genetic programming in python, with a scikit-learn inspired API (2016), https://gplearn.readthedocs.io/ [Last accessed on 8 Jun 2022]
135. Collette Y, Hansen N, Pujol G, Salazar Aponte D, Le Riche R. In multidisciplinary design optimization in computational mechanics (2013), pp. 499. DOI
136. S. Mirjalili. in Evolutionary algorithms and neural networks: theory and applications, edited by Seyedali Mirjalili. Springer International Publishing: Cham; 2019. pp. 43. DOI
137. Whitley D. A genetic algorithm tutorial. *Stat Comput* 1994;4. DOI
138. Ferri F, Pudil P, Hatef M, Kittler J. Comparative study of techniques for large-scale feature selection. Comparative Studies and Hybrid Systems. Elsevier; 1994. pp. 403-13. DOI
139. Baraniuk R. Compressive sensing [Lecture Notes]. *IEEE Signal Process Mag* 2007;24:118-21. DOI
140. L. Breiman, J. H. Friedman, and R. A. Olshen, Classification and regression trees. (Wadsworth International Group, Belmont, CA, 1984). DOI
141. Wen Y, Fu L, Li G, Ma J, Ma H. Accelerated discovery of potential organic dyes for dye-sensitized solar cells by interpretable machine learning models and virtual screening. *Sol RRL* 2020;4:2000110. DOI

142. Shapley LS. A value for n-person games. (Contrib. Theor. Games, 1953). DOI
143. Zhang S, Lu T, Xu P, Tao Q, Li M, Lu W. Predicting the formability of hybrid organic-inorganic perovskites via an interpretable machine learning strategy. *J Phys Chem Lett* 2021;12:7423-30. DOI PubMed
144. Guolin K, Qi M, Thomas F, Taifeng W, et al. In advances in neural information processing systems 30 (NIPS 2017) (Long Beach, CA, USA, 2017). DOI
145. Paszke A, Gross S, Massa F, et al. PyTorch: an imperative style, high-performance deep learning library. (Curran Associates, Inc, 2019), pp. 8024. Available from: https://proceedings.neurips.cc/paper/2019/file/bdbca288fee7f92f2bfa9f7012727740-Paper.pdf [Last accessed on 13 Jun 2022]
146. M. Abadi, A. Agarwal, P. Barham, et al. TensorFlow: large-scale machine learning on heterogeneous systems (2015). Available from: https://arxiv.org/abs/1603.04467 [Last accessed on 13 Jun 2022]
147. Zárate Hernández LA, Camacho-Mendoza RL, González-Montiel S, Cruz-Borbolla J. The chemical reactivity and QSPR of organic compounds applied to dye-sensitized solar cells using DFT. *J Mol Graph Model* 2021;104:107852. DOI PubMed
148. Wu Y, Guo J, Sun R, Min J. Machine learning for accelerating the discovery of high-performance donor/acceptor pairs in non-fullerene organic solar cells. *npj Comput Mater* 2020;6. DOI
149. David TW, Anizelli H, Tyagi P, Gray C, Teahan W, Kettle J. Using large datasets of organic photovoltaic performance data to elucidate trends in reliability between 2009 and 2019. *IEEE J Photovoltaics* 2019;9:1768-73. DOI
150. Kar S, Roy J, Leszczynska D, Leszczynski J. Power conversion efficiency of arylamine organic dyes for dye-sensitized solar cells (DSSCs) explicit to cobalt electrolyte: understanding the structural attributes using a direct QSPR approach. *Computation* 2017;5:2. DOI
151. Roy JK, Kar S, Leszczynski J. Insight into the optoelectronic properties of designed solar cells efficient tetrahydroquinoline dye-sensitizers on TiO2(101) surface: first principles approach. *Sci Rep* 2018;8:10997. DOI PubMed PMC
152. Roy JK, Kar S, Leszczynski J. Electronic structure and optical properties of designed photo-efficient indoline-based dye-sensitizers with D-A-π-A framework. *J Phys Chem C* 2019;123:3309-20. DOI
153. Roy K, Ambure P, Kar S, Ojha PK. Is it possible to improve the quality of predictions from an “intelligent” use of multiple QSAR/QSPR/QSTR models?: quality of predictions from an “intelligent” use of multiple models. *J Chemom* 2018;32:e2992. DOI
154. Cramer J. The origins of logistic regression. *SSRN J* . DOI
155. Tolles J, Meurer WJ. Logistic regression: relating patient characteristics to outcomes. *JAMA* 2016;316:533-4. DOI PubMed
156. Walker SH, Duncan DB. Estimation of the probability of an event as a function of several independent variables. *Biometrika* 1967;54:167. PubMed
157. Yu Y, Tan X, Ning S, Wu Y. Machine learning for understanding compatibility of organic-inorganic hybrid perovskites with post-treatment amines. *ACS Energy Lett* 2019;4:397-404. DOI
158. J. Friedman, T. Hastie, and R. Tibshirani. Regularization paths for generalized linear models via coordinate descent. *J Stat Softw* 2010;33 DOI
159. Santosa F, Symes WW. Linear inversion of band-limited reflection seismograms. *SIAM J Sci and Stat Comput* 1986;7:1307-30. DOI
160. Hoerl AE, Kennard RW. Ridge regression: biased estimation for nonorthogonal problems. *Technometrics* 1970;12:55-67. DOI
161. Li X, Dan Y, Dong R, et al. Computational screening of new perovskite materials using transfer learning and deep learning. *Appl Sci* 2019;9:5510. DOI
162. Stoddard RJ, Dunlap-shohl WA, Qiao H, Meng Y, Kau WF, Hillhouse HW. Forecasting the decay of hybrid perovskite performance using optical transmittance or reflected dark-field imaging. *ACS Energy Lett* 2020;5:946-54. DOI
163. Padula D, Simpson JD, Troisi A. Combining electronic and structural features in machine learning models to predict organic solar cells properties. *Mater Horiz* 2019;6:343-9. DOI
164. Wu X, Kumar V, Ross Quinlan J, et al. Top 10 algorithms in data mining. *Knowl Inf Syst* 2008;14:1-37. DOI
165. Raccuglia P, Elbert KC, Adler PD, et al. Machine-learning-assisted materials discovery using failed experiments. *Nature* 2016;533:73-6. DOI PubMed
166. Jiménez-luna J, Grisoni F, Schneider G. Drug discovery with explainable artificial intelligence. *Nat Mach Intell* 2020;2:573-84. DOI
167. Breiman L. Pasting small votes for classification in large databases and on-line. *Machine Learning* 1999; 36:85-103. DOI
168. Breiman L. Bagging predictors. *Mach Learn* 1996;24:123-40. DOI
169. Tin Kam Ho. The random subspace method for constructing decision forests. *IEEE Trans Pattern Anal Machine Intell* ;20:832-44. DOI
170. Louppe G, Geurts P. Ensembles on random patches. (Springer Berlin Heidelberg, Berlin, Heidelberg, 2012), pp. 346. Available from: https://link.springer.com/chapter/10.1007/978-3-642-33460-3_28 [Last accessed on 13 Jun 2022]
171. Takahashi K, Takahashi L, Miyazato I, Tanaka Y. Searching for hidden perovskite materials for photovoltaic systems by combining data science and first principle calculations. *ACS Photonics* 2018;5:771-5. DOI
172. Freund Y, Schapire RE. A decision-theoretic generalization of on-line learning and an application to boosting. *J Comput and Sys Sci* 1997;55:119-39. DOI
173. J. H. Friedman, Greedy function approximation: a gradient boosting machine. *Ann. Stat* 2001; 29, 1189 (2001), DOI
174. G. Ke, Q. Meng, T. Finley, T. Wang, W. Chen, W. Ma, Q. Ye, and T.-Y. Liu, in Proceedings of the 31st International Conference on Neural Information Processing Systems (Curran Associates Inc., Long Beach, California, USA, 2017), pp. 3149. DOI
175. Prokhorenkova L, . Gusev G, A. Vorobev, A. V. Dorogush, A. Gulin. CatBoost: unbiased boosting with categorical features. Available from: https://arxiv.org/abs/1706.09516 [Last accessed on 13 Jun 2022]
176. Sahu H, Ma H. Unraveling correlations between molecular properties and device parameters of organic solar cells using machine learning. *J Phys Chem Lett* 2019;10:7277-84. DOI PubMed

177. Cortes C, Vapnik V. Support-vector networks. *Mach Learn* 1995;20:273-97. DOI
178. Smola AJ, Schölkopf B. A tutorial on support vector regression. *Stat Comput* 2004;14:199-222. DOI
179. Wu T, Wang J. Global discovery of stable and non-toxic hybrid organic-inorganic perovskites for photovoltaic systems by combining machine learning method with first principle calculations. *Nano Energy* 2019;66:104070. DOI
180. Ambikasaran S, Foreman-Mackey D, Greengard L, Hogg DW, O'Neil M. Fast direct methods for gaussian processes. *IEEE Trans Pattern Anal Mach Intell* 2016;38:252-65. DOI
181. Rasmussen CE, Williams CKI. Gaussian processes for machine learning. The MIT Press, 2006. DOI
182. Pyzer-knapp EO, Simm GN, Aspuru Guzik A. A Bayesian approach to calibrating high-throughput virtual screening results and application to organic photovoltaic materials. *Mater Horiz* 2016;3:226-33. DOI
183. Li J, Pradhan B, Gaur S, Thomas J. Predictions and strategies learned from machine learning to develop high-performing perovskite solar cells. *Adv Energy Mater* 2019;9:1901891. DOI
184. Sanchez-Lengeling B, Aspuru-Guzik A. Inverse molecular design using machine learning: generative models for matter engineering. *Science* 2018;361:360-5. DOI PubMed
185. Creswell A, White T, Dumoulin V, Arulkumaran K, Sengupta B, Bharath AA. Generative adversarial networks: an overview. *IEEE Signal Process Mag* 2018;35:53-65. DOI
186. Goodfellow I, Pouget-abadie J, Mirza M, et al. Generative adversarial networks. *Commun ACM* 2020;63:139-44. Available from: https://proceedings.neurips.cc/paper/2014/hash/5ca3e9b122f61f8f06494c97b1afccf3-Abstract.html [Last accessed on 13 Jun 2022]
187. Goodfellow I J, Pouget-Abadie J, Mirza M, et al. Generative Adversarial Networks. 2014. Available from: https://arxiv.org/abs/1406.2661 [Last accessed on 13 Jun 2022]
188. Kingma D P, Welling M. Auto-encoding variational bayes. Available from: https://arxiv.org/abs/1312.6114 [Last accessed on 13 Jun 2022]
189. Rousseeuw PJ. Silhouettes: a graphical aid to the interpretation and validation of cluster analysis. *J Comput Appl Math* 1987;20:53-65. DOI
190. Choudhary K, Bercx M, Jiang J, Pachter R, Lamoen D, Tavazza F. Accelerated discovery of efficient solar-cell materials using quantum and machine-learning methods. *Chem Mater* 2019;31:5900-8. DOI PubMed PMC
191. Komer B, Socastro MT, Kim W. Hyperopt: distributed hyperparameter optimization (2012-2021). Available from: https://github.com/hyperopt/hyperopt [Last accessed on 9 Jun 2022]
192. Akiba T, Sano S, Yanase T, Ohta T, Koyama M. A next-generation hyperparameter optimization framework. Preferred Networks, Inc., 2017-2021. DOI
193. Liaw R, Liang E, Nishihara R, Moritz P, Gonzalez JE, Stoica I. tune: scalable hyperparameter tuning (The Ray Team, 2018). Available from: https://docs.ray.io/en/latest/tune/index.html [Last accessed on 10 Jun 2022]
194. Lu S, Zhou Q, Ma L, Guo Y, Wang J. Rapid discovery of ferroelectric photovoltaic perovskites and material descriptors via machine learning. *Small Methods* 2019;3:1900360. DOI
195. Kim C, Pilania G, Ramprasad R. Machine learning assisted predictions of intrinsic dielectric breakdown strength of ABX3 perovskites. *J Phys Chem C* 2016;120:14575-80. DOI
196. Körbel S, Marques MAL, Botti S. Stability and electronic properties of new inorganic perovskites from high-throughput ab initio calculations. *J Mater Chem C* 2016;4:3157-67. DOI
197. Gómez-Bombarelli R, Aguilera-Iparraguirre J, Hirzel TD, et al. Design of efficient molecular organic light-emitting diodes by a high-throughput virtual screening and experimental approach. *Nat Mater* 2016;15:1120-7. DOI PubMed
198. Tao Q, Lu T, Sheng Y, Li L, Lu W, Li M. Machine learning aided design of perovskite oxide materials for photocatalytic water splitting. *J Energy Chem* 2021;60:351-9. DOI
199. Xu P, Lu T, Ju L, Tian L, Li M, Lu W. Machine learning aided design of polymer with targeted band gap based on DFT computation. *J Phys Chem B* 2021;125:601-11. DOI PubMed
200. Jin H, Zhang H, Li J, et al. Discovery of novel two-dimensional photovoltaic materials accelerated by machine learning. *J Phys Chem Lett* 2020;11:3075-81. DOI PubMed
201. Rajagopal A, Yao K, Jen AK. Toward perovskite solar cell commercialization: a perspective and research roadmap based on interfacial engineering. *Adv Mater* 2018;30:e1800455. DOI PubMed
202. Li Z, Klein TR, Kim DH, et al. Scalable fabrication of perovskite solar cells. *Nat Rev Mater* 2018;3. DOI PubMed
203. Zhou G, Chu W, Prezhdo OV. Structural deformation controls charge losses in $MAPbI_3$: unsupervised machine learning of nonadiabatic molecular dynamics. *ACS Energy Lett* 2020;5:1930-8. DOI
204. Kennard RW, Stone LA. Computer Aided design of experiments. *Technometrics* 1969;11:137-48. DOI
205. Park H, Jun C. A simple and fast algorithm for K-medoids clustering. *Expert Syst Appl* 2009;36:3336-41. DOI
206. Ertl P, Schuffenhauer A. Estimation of synthetic accessibility score of drug-like molecules based on molecular complexity and fragment contributions. *J Cheminform* 2009;1:8. DOI PubMed PMC
207. Venkatraman V, Yemene AE, de Mello J. Prediction of absorption spectrum shifts in dyes adsorbed on titania. *Sci Rep* 2019;9:16983. DOI PubMed PMC
208. Isida fragmentor. Available from: http://infochim.u-strasbg.fr/downloads/manuals/Fragmentor2017/Fragmentor2017_Manual_nov2017.pdf [Last accessed on 13 Jun 2022]
209. Cooper CB, Beard EJ, Vázquez-mayagoitia Á, et al. Design-to-device approach affords panchromatic co-sensitized solar cells. *Adv Energy Mater* 2019;9:1802820. DOI

210. Swain MC, Cole JM. ChemDataExtractor: a toolkit for automated extraction of chemical information from the scientific literature. *J Chem Inf Model* 2016;56:1894-904. DOI PubMed

211. Lee M. Insights from machine learning techniques for predicting the efficiency of fullerene derivatives-based ternary organic solar cells at ternary blend design. *Adv Energy Mater* 2019. DOI

212. Zhao Z, del Cueto M, Geng Y, Troisi A. Effect of increasing the descriptor set on machine learning prediction of small molecule-based organic solar cells. *Chem Mater* 2020;32:7777-87. DOI

213. Meftahi N, Klymenko M, Christofferson AJ, Bach U, Winkler DA, Russo SP. Machine learning property prediction for organic photovoltaic devices. *npj Comput Mater* 2020;6. DOI

214. Carbonell P, Carlsson L, Faulon JL. Stereo signature molecular descriptor. *J Chem Inf Model* 2013;53:887-97. DOI PubMed

215. Scharber M, Mühlbacher D, Koppe M, et al. Design rules for donors in bulk-heterojunction solar cells-towards 10 % energy-conversion efficiency. *Adv Mater* 2006;18:789-94. DOI

216. Winkler DA, Burden FR. Robust QSAR models from novel descriptors and bayesian regularised neural networks. *Mol Simul* 2006;24:243-58. DOI

217. Lucic B, Amic D, Trinajstic N. Nonlinear multivariate regression outperforms several concisely designed neural networks on three QSPR data sets. *J Chem Inf Comput Sci* 2000;40:403-13. DOI PubMed

218. David TW, Anizelli H, Jacobsson TJ, Gray C, Teahan W, Kettle J. Enhancing the stability of organic photovoltaics through machine learning. *Nano Energy* 2020;78:105342. DOI

219. Reese MO, Gevorgyan SA, Jørgensen M, et al. Consensus stability testing protocols for organic photovoltaic materials and devices. *Sol Energy Mater Sol Cells* 2011;95:1253-67. DOI

220. Flake GW, Lawrence S. .Efficient SVM regression training with SMO. *Machine Learning* 2002;46:271-90. DOI

221. Du X, Lüer L, Heumueller T, et al. Elucidating the full potential of OPV materials utilizing a high-throughput robot-based platform and machine learning. *Joule* 2021;5:495-506. DOI

222. Quinlan JR. Induction of decision trees. *Mach Learn* 1986;1:81-106. DOI

223. J. R. Quinlan, C4.5: Programs for machine learning. *Mach Learn* 1994;16:235-240. DOI

224. Lu T, Li H, Li M, Wang S, Lu W. Predicting experimental formability of hybrid organic-inorganic perovskites via imbalanced learning. *J Phys Chem Lett* 2022;13:3032-8. DOI PubMed

225. Im J, Lee S, Ko T, Kim HW, Hyon Y, Chang H. Identifying Pb-free perovskites for solar cells by machine learning. *npj Comput Mater* 2019;5. DOI

226. Sun S, Hartono NT, Ren ZD, et al. Accelerated development of perovskite-inspired materials via high-throughput synthesis and machine-learning diagnosis. *Joule* 2019;3:1437-51. DOI

227. Lu S, Zhou Q, Ouyang Y, Guo Y, Li Q, Wang J. Accelerated discovery of stable lead-free hybrid organic-inorganic perovskites via machine learning. *Nat Commun* 2018;9:3405. DOI PubMed PMC

228. Li Z, Xu Q, Sun Q, Hou Z, Yin W. Thermodynamic stability landscape of halide double perovskites via high-throughput computing and machine learning. *Adv Funct Mater* 2019;29:1807280. DOI

229. Schmidt J, Shi J, Borlido P, Chen L, Botti S, Marques MAL. Predicting the thermodynamic stability of solids combining density functional theory and machine learning. *Chem Mater* 2017;29:5090-103. DOI

230. Venkatraman V, Foscato M, Jensen VR, Alsberg BK. Evolutionary de novo design of phenothiazine derivatives for dye-sensitized solar cells. *J Mater Chem A* 2015;3:9851-60. DOI

231. Majeed N, Saladina M, Krompiec M, Greedy S, Deibel C, Mackenzie RCI. Using deep machine learning to understand the physical performance bottlenecks in novel thin-film solar cells. *Adv Funct Mater* 2020;30:1907259. DOI

232. Pokuri BSS, Ghosal S, Kokate A, Sarkar S, Ganapathysubramanian B. Interpretable deep learning for guided microstructure-property explorations in photovoltaics. *npj Comput Mater* 2019;5. DOI

233. Sahu H, Yang F, Ye X, Ma J, Fang W, Ma H. Designing promising molecules for organic solar cells via machine learning assisted virtual screening. *J Mater Chem A* 2019;7:17480-8. DOI

234. Sahu H, Rao W, Troisi A, Ma H. Toward predicting efficiency of organic solar cells via machine learning and improved descriptors. *Adv Energy Mater* 2018;8:1801032. DOI

235. Padula D, Troisi A. Concurrent optimization of organic donor-acceptor pairs through machine learning. *Adv Energy Mater* 2019;9:1902463. DOI

236. Nagasawa S, Al-Naamani E, Saeki A. Computer-aided screening of conjugated polymers for organic solar cell: classification by random forest. *J Phys Chem Lett* 2018;9:2639-46. DOI PubMed